2019

Quantification of porosity and its effects on the quasi-static and dynamic behavior of the additively manufactured nickel-based superalloy Inconel 718

Andrew Minor

Quantification of Porosity and its Effects on the Quasi-Static and Dynamic Behavior of the Additively Manufactured Nickel-Based Superalloy Inconel 718

CREATED BY

ANDREW MINOR

The University of Alabama in Huntsville

Submitted in partial fulfillment of the requirements for the degree of Master of Science in Engineering
in
The Department of Mechanical and Aerospace Engineering
to
The School of Graduate Studies
of
The University of Alabama in Huntsville
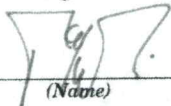
THESIS COPY PERMISSION PAGE

In presenting this thesis in partial fulfillment of the requirements for a master's degree from The University of Alabama in Huntsville, I agree that the Library of this University shall make it freely available for inspection. I further agree that permission for extensive copying for scholarly purposes may be granted by my advisor or, in his/her absence, by the Chair of the Department or the Dean of the School of Graduate Studies. It is also understood that due recognition shall be given to me and to The University of Alabama in Huntsville in any scholarly use which may be made of any material in this thesis.

_____ 3/14/2019
(Student Signature)   (Date)

I

THESIS APPROVAL FORM

Submitted by Andrew Minor in the partial fulfillment of the requirements for the degree of Masters of Science in Mechanical Engineering and accepted on behalf of the Faculty of the School of Graduate Studies by the thesis committee.

We, the undersigned members of the Graduate Faculty of The University of Alabama in Huntsville, certify that we have advised and/or supervised the candidate of the work described in this thesis. We further certify that we have reviewed the thesis and approve it in partial fulfillment of the requirements of the degree of Masters of Science in Mechanical Engineering.

_____ 3/6/19 Thesis Committee Chair
(Name)   (Date)

_____ 3/6/19 Thesis Committee
(Name)   (Date)

_____ 3/6/19 Thesis Committee
(Name)   (Date)

_____ 3/26/19 Department Chair
(Name)   (Date)

_____ 03/29/19 College Dean
(Name)   (Date)

_____ 4/8/19 Graduate Dean
(Name)   (Date)

II
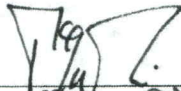
ABSTRACT APPROVAL

_____   6 Mar 2019   Committee Chair
        Name   (Date)

_____   3/26/19   Department Chair
        Name   (Date)

_____   _____   Graduate Dean
        Name   (Date)

IV

Acknowledgments

Last, but certainly not least, I could not have been able to accomplish anything without my Lord and Savior Jesus Christ, my family, and friends. Thank you for always being there and pushing me through the hard times. Without you, none of this would have been possible.

Contents

List of Figures

List of Tables

Chapter 1

Additive Manufacturing

This chapter introduces additive manufacturing (AM) and the impact it's having on manufacturing and related technologies. Commercially available AM processes are briefly reviewed with a particular emphasize on the specific process chosen for this study. Following the processes is a discussion on the advantages and challenges of AM. The advantages outweigh the challenges but in the end, there are still improvements that need to be made in order to address some of the challenges presented in this chapter. This study aims specifically to find a correlation between porosity that emerges during the manufacturing process in conjunction with following post-processing heat treatments on the subsequent mechanical behavior. Findings from this investigation provide new insights on the allowable amount of porosity at different states of stress.

1.1   Introduction to Additive Manufacturing

Innovation in manufacturing technologies and concepts is limitless on the possibilities of creativity and design. Although, innovation has been hindered by the long-standing question: How can we make this concept come to life? The vast engineering minds that dreamed up the rockets, automobiles, cell phones, etc. are always churning out new ideas that should not be bound by manufacturing techniques. Traditional manufacturing (TM) techniques and speed to market are considerations that can be difficult to overcome. With manufacturing affecting nearly every facet of everyday life, the manufacturing industry is rapidly growing with AM at the forefront of innovation [10, 11].

AM is making a tremendous, positive impact on society by improving everyday uses such as automobiles, airplanes, buildings, etc. by allowing designers and manufactures to have more freedom when creating complex structures. As technology progresses, AM parts move from the prototype phase onto the production line. There is a large investment of AM in the aerospace industry. In 2015, NASA integrated AM on a fuel turbopump, fuel injector, valves and several other major components on an engine prototype, along with the first actual-size copper (Cu) rocket engine part [12]. In 2016, GE integrated AM into the fuel nozzles of their LEAP family of engines that reduced the nozzle weight by 25%, reduced the number of parts from 18 to 1, and integrated more cooling pathways and supports, increasing the efficiency and durability [12]. The medical field is also utilizing AM by expanding the field of personalized medicine. For example, patient customized implants that are difficult to make by TM can be AM at a lower cost, faster rate, and easier [13]. AM aligns with the needs of the automotive industry with Ford implementing AM printed brake parts for the 2019 Shelby Mustang GT500, BMW recently printed their one millionth part being a window

1

guide rail for the BMW i8 Roadster, and NASCAR and Formula One are starting to adopt AM to make a lighter, more durable race car [14]. AM will continue to pave the way for innovation and continue to radically change the manufacturing industry.

1.2   Additive Manufacturing Processes

In order to transform the metal powder into a dense three-dimensional (3D) part, an AM process must first be chosen. All metal AM processes achieve this goal by either solid-state joining or melting. An ASTM standard F2792-12a for processing terminology was created and the following are relevant to metal AM [15]:

- Sheet Lamination

- Binder Jetting

- Direct Energy Deposition

- Powder Bed Fusion

Within these four different AM processes, there are different techniques that are discussed in further detail below with an emphasis on powder bed fusion (PBF) since that is the process used for this study.

1.2.1   Sheet Lamination

Sheet lamination (SL) is an AM process that bonds two sheets of metal together. An SL technique for joining sheets of metal together by ultrasonic welding is ultrasonic AM (UAM)[16]. This welding is at a low temperature and does not melt the material but merely softens the material and when cooled, the layers adhere. The standard procedure for UAM is to stack a sheet of metal on top of a previous sheet, weld the sheets together, then cut out the desired shape [16]. This process will repeat until the final structure is complete. This technique offers several advantages including creating internal geometries to go into existing structures, speed of the process, and low cost. On the contrary, UAM requires additional machining to cut out the design and is limited on the materials that can be used [17].

1.2.2   Binder Jetting

The binder jetting (BJ) process deposits a liquid binding agent (binder) on the metal powder causing the adhesive to conjoin the metal powder together to create the part. The BJ process begins by rolling a thin layer of metal powder material into the build plate, utilizes an inkjet print head to strategically deposit the binder onto the metal powder, the build plate then lowers while an additional layer of metal powder is spread over the previously adhered layer, then the process repeats[18]. One unique quality of BJ is that there is no heat used during the process. Because of this, the finished part still has loose powder and is only about 60% dense [19]. As a result, several post-processing heat treatments are required before the part can go into service. But, a positive to no heat being used during the process is that there are little to no internal stresses within the part [18].

1.2.3 Direct Energy Deposition

Direct energy deposition (DED) is a metal AM process that embodies all techniques where focused energy generates a melt pool and then filled with either metal powder or wire. One of the more common DED techniques is called powder-fed where a laser generates a melt pool and the metal powder is deposited [19]. A similar technique is using a wire to fill the molten pool instead of powder called wire-fed [19]. The powder or wire feed can be co-located in the nozzle of the energy source, or it can be deposited from a separate head. The DED process uses a multi axis arm to guide a nozzle that deposits the metal powder onto the build plate as the arm traces the design of the part. This process gives the ability to control the microstructure to a high degree resulting in high quality of the finished product [20]. By controlling the speed of the axis arm, a pre-determined microstructure can be obtained [21]. The limiting factor in DED is the limited material that can be used because metals that has a high thermal conductivity and reflectivity such as gold, Cu, and some aluminum (Al) alloys, are hard to process [22].

1.2.4 Powder Bed Fusion

Powder bed fusion (PBF), which is the process used in this study, encompasses every technique where a focused energy beam melts a powder bed of metal material layer-by-layer to build a component. There are several different PBF processes including electron beam melting (EBM), selective laser sintering (SLS), and selective laser melting (SLM). Like its name suggests, in the EBM process, an electron beam is used to melt the metal powder in a layer-by-layer fashion by using a heated tungsten filament that emits electrons at high speed which are then controlled by two magnetic fields, focus coil and deflection coil [23]. When the electrons hit the metal powder, their kinetic energy gets converted into thermal energy causing the powder to melt [24]. In the SLS process, the metal powder is selectively fused together by one or more lasers in an enclosed chamber [23]. A more advanced form of the SLS process, and the AM process used for this study, is the SLM process. A schematic of this process is shown in Figure 1.1. The SLM technique uses a computer-aided design (CAD) that is later converted to a stereolithography (STL) file to guide the laser path. A build plate is required to provide structural support for the component as it is being built. The first step towards building occurs by adding a thin layer of the metal powder onto the build plate. The laser, guided by the CAD model, then traces the first layer of the component, melting this layer onto the build plate. Once the first layer is complete, the build plate lowers and a new powder layer is added on top of the first layer. This process repeats until the entire component is complete. The laser depth penetrates several layers of the powdered material causing the preceding layer to also melt allowing the layers to bond together. As a result, small melt volumes form and rapidly solidify due to the scanning speed. Once the SLM procedure is complete, the excess powder can be reused for future parts. This process allows for high quality parts due to being able to control the heat and scan speed of the process resulting in microstructure control, and superb surface quality [21]. The SLM process has proven its capabilities with several high-strength materials, including Inconel 718 (IN718) [21, 25, 26].

3
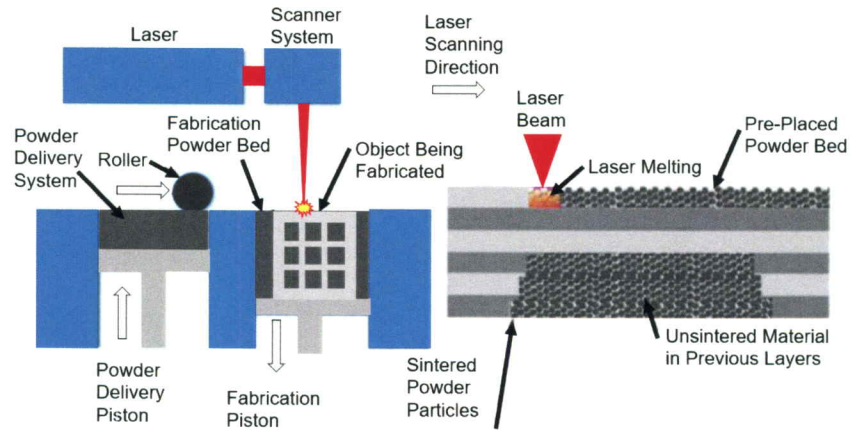
Figure 1.1: Visualization of the selective laser melting (SLM) process [1]

1.3 Advantages of Additive Manufacturing

AM is destined to address TM hurdles such as the inability to produce complex components and increased cost, allowing inventors and industries to have more freedom to create structures not possible in TM. Reason being, AM offers several advantages over TM. Some of which include, but not limited to, ease of producing complex components, cost effective, faster production, reduced waste, and better control over the elements in your material. These advantages are discussed in more detail below.

1.3.1 Complex Components

The design freedoms offered by AM allow existing products and components to be redesigned to optimize applicability. Manufacturing complex components by TM has always been a difficult, strenuous process requiring excellent precision and skill. For instance, when creating lattice structures (LS), it is virtually impossible to do so using traditional methods due to the physical structure varying as well as channels of air throughout the component as shown in Figure 3.5. AM solves these problems by removing the need to assemble multiple individual parts by creating the whole structure in one process.

1.3.2 Cost Effective

Numerous multi-component parts created by TM can be substituted by an AM part comprising of one coherent component, minimizing the cost, time and quality issues as a result of TM fabrication processes. The assembly cost is minimized through combining multiple parts into a single, more effective whole. Redesigning existing parts that are TM and the outcome becomes an ideal strength-to-weight ratio capable of reaching the functional necessities while minimizing material volume which reduces the cost [27]. By reducing the weight of components, a reduction on energy consumption is capable of saving $56–219 billion by 2025 [28]. Life cycle studies have been conducted proving that AM is estimated to save $113–370 billion by 2025 by saving in the production of goods by reducing the material, resulting in shorter supply chains [28]. The economic benefits as a result of AM processing improvements and efficiency compared to TM are greater than the benefits from the avoidance of investment in tooling [29]. Once the part design is finalized, fabrication can immediately begin resulting in cost savings by removing the time between the processes to produce more parts.

4

1.3.3 Faster Production

The adaptability with which new models can be altered can reduce the time from design to production. Faster time to market means a quicker turn on investment. Traditional manufacturing technologies require molds to be manufactured and factories to be ramped up to speed, resulting in taking days even months to have the first part in hand [30]. Not only is this process time consuming, the longer the part is in production, the more money is lost through manufacturing costs and a slow turn on investment.

1.3.4 Reduced Waste

AM generates significantly less waste than TM. For example, a milling machine removes material from a large block of material to create the final product [31]. The material that is removed usually cannot be reused and ends up wasted. Alternatively, during AM, the only material consumed is what comes in contact with the laser so only the material that is required gets used. The powdered material that doesn't get used can be reused in other parts. Studies have shown that AM can be used to manufacture and maintain the rotor and disk blades on a turbine and reduce waste with about 60% savings on material and about 30% savings in time [32].

1.3.5 Elemental Control

Recent efforts in AM of materials have been focusing on bringing multiple unique elements, designs, and/or properties into one part [33, 34]. For example, nature builds and grows the living world around us from a few basic elements. The refined combination of often frail, multipurpose constituents results in excellent functional properties. With maturing AM technologies that allow unmatched control over material properties at microscopic levels by being able to control processing parameters such as heat and scan speed, the tools required for outdoing the TM design strategy in metallic structures is increasing [1]. AM can potentially engineer materials at an elemental level, contrary to the purely mechanical TM process. The convolution of the AM process — where materials can be broken down into component forms in order to ease the additive nature of the process — has great potential for modifying the material qualities of a particular metal [35].

AM has great potential to influence production. By having more design freedom and not being limited by TM, the design of parts can be changed to incorporate more complex structures, which directly affects the following stages of production and can lead to manufacturing and design breakthroughs. Although TM will never be replaced, AM will compliment and improve the quality of the overall product. By knowing these advantages of AM, it will be easier for innovators, designers and manufacturers to advance in their respected fields.

1.4 Challenges of Additive Manufacturing

Despite all the advantages, there are still challenges within AM that need to be overcome before widespread adoption. Several AM studies on identifying the most important industrial challenges have been conducted, including efforts sponsored by the National Science Foundation and the National Institute of Standards and Technology [36]. Due to the layer-by-layer fabrication nature of AM, large thermal gradients and voids are prone to occur that causes significant departure of underlying microstructure from TM. Some criti-

cal challenges additive methods face are residual stresses, nonuniform microstructure, and porosity, which are described in further detail below.

1.4.1 Residual Stress

Residual stresses are self-equilibrating internal stresses existing in a free body, which has no external forces or constraints on its boundaries. If this internal stress is higher than the yield strength of the material, warping and plastic deformation can occur. Likewise, if this internal stress exceeds the ultimate tensile strength of the material, cracking may occur. The magnitude and distribution of AM residual stress varies with process parameters such as construction rate, scanning speed, and temperature [37]. It is reported that the temperature gradient that is generated from the rapid heating beneath the laser beam compared to the slow heat conduction in the sample leads to localized compressive and tensile forces, which in turn, give rise to residual stresses [37, 38, 39]. Residual stresses can negatively affect the integrity and lifespan of components. For materials that can be plastically deformed, residual stresses may enhance or delay the transition from elastic to plastic deformation because the applied stress and the residual stress are directly added together until the yield point is achieved [38]. Sasahara concluded that residual stress can raise or lower the mean stress experienced over a fatigue cycle in 0.45% carbon steel [40]. Ebert identified that fatigue failures in 1061 steel may occur in structures that would otherwise be immune to fatigue fracture if tensile residual stresses are present in areas of high cyclic stress loading, yet the failure will be attributed to fatigue [41]. In general, if the material is subjected to residual stresses, when the part encounters another external stress, the residual stress and the external stress components get added together and the part is locally overloaded and fails as a result of the residual stress [42].

Several techniques have been developed in order to quantify residual stress in AM samples. These techniques are grouped together as non-destructive (X-ray diffraction, ultrasonic velocity, and Barkhausen noise analysis) or destructive (hole drilling, splitting and block removal) [43]. Destructive testing damages or removes a section of material so that the sample can no longer be used. However, they all have a common trait, that is, being indirect. There is no direct method available to measure stresses. They are calculated or derived from a measured quantity such as elastic strain or displacement [44]. The more common ways to measure residual stresses in AM parts are through non-destructive methods, specifically neutron diffraction and X-ray diffraction [45, 46]. It is important to know how to quantify residual stress in order to aid researchers on selecting the proper techniques depending on their application. It is also important to be able to quantify residual stress so the AM process can be altered in order to minimize residual stress to optimize the mechanical properties of the finished product.

1.4.2 Nonuniform Microstructure

For AM AB components, the grain structures are unique in the fact that columnar grains are dominate [19]. Similar to any other fabrication processes, microstructural features of SLM parts such as grain morphology (size and shape) [47] and texture [48] is prone to change by the laser scan parameter/strategy and the subsequent thermal cycles. Residual stress can also effect the microstructure from the standpoint that altering the scan strategies in order to avoid it acts as a driving force for heterogeneous recrystallisation [19].

Microstructure is the most important aspect of any engineering material, therefore, studying the microstructure of a material provides information about a direct linkage be-

tween the processing to the properties and performance [49]. Zhang et al. studied the microstructural characteristics and dominant microstructural factors governing mechanical properties of a titanium (Ti)-based superalloy containing Aluminium (Al) and Vanadium (V) (Ti-6Al-4V) concluding that the mechanical properties were heterogeneously distributed in the weld, which were directly related with the heterogeneous distribution of microstructure [4]. Filip et al. showed that the fracture toughness of Ti–6Al–2(molybdenum) Mo–2(chromium)Cr alloy through tensile loading can be increased by adjusting and improving the microstructure through proper heat treatment. Their study also showed that the proof stress increases due to continuous refinement of the microstructure, reducing the slip length, resulting in a maximum tensile elongation [50]. Tasan et al. identified connections between strain and damage heterogeneity and the underlying microstructural parameters by conducting *in situ* deformation experiments on two different dual phase steel grades, employing two different microscopic-digital image correlation (MDIC) techniques to achieve microstructural strain maps of representative statistics and high-resolution [2]. The analyses carried out in this study revealed that the larger ferrite grains typically plastically deform earlier than smaller grains, therefore, they act as the initial deformation nodes in the developing microstructural strain network, resulting in deformation by the formation of high deformation bands connecting these nodes. Also, damage incidents are observed at the boundaries of these highly deformed zones and the surrounding microstructure, which is obvious for coarser microstructure with more homogeneously distributed, smaller martensite islands. Finally, while in microstructure regions with well-dispersed martensite islands, majority of the ferritic regions are observed to contribute to strain accommodation and hardening, for other microstructures with bulky martensites wider localization bands are developed, the position and propagation of which is primarily governed by the position of the bulky martensite islands, possibly leading also to earlier macroscopic strain localization [2]. Figure 1.2 shows the results from testing coarse grain (CG), fine grain (FG), and ultra-fine grain (UFG) dual phase steel from Tasan's work. As the microstructure changes from coarse grain (CG) to ultra-fine grain (UFG), the yield point and the flow stress increases by around 19%. This illustrates that the mechanical properties are directly related to the microstructure [2]. Microstructure can cause your material to have outstanding, or detrimental mechanical properties as displayed above, therefore it is important to be able to understand the effects, and know what the optimal microstructure is for maximum performance of the part.

7
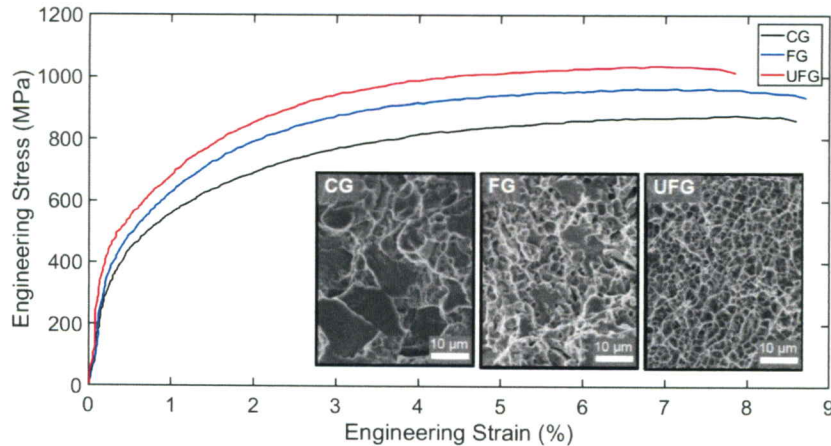
Figure 1.2: Engineering stress vs engineering strain plot for dual phase steel for coarse grain (CG), fine grain (FG), and ultra-fine grain (UFG) microstructures. An image of the various microstructures are also shown [2].

There are many different methods available in order to quantify the microstructure. Some of the more popular methods are optical and electron microscopy. Optical microscopy is a technique used to closely view a sample through the magnification of a lens with visible light. A single lens or a series of lenses are placed between the sample and the viewer's eye to magnify the image while a light illuminates the sample so that it can be examined in greater detail [51]. Once the desired microstructure is observed, an image can be taken to record the data. This easy-to-use method is desired when determining the grain structure on the surface of your sample. If a greater depth of field or a higher magnification is required, scanning electron microscopy (SEM) is another method to quantify microstructure. Scanning electron microscopy uses a beam of electrons directed at a sample to obtain a surface image [52]. Scanning electron microscopy is useful when observing surface topography and analysis of fracture surfaces along with composition analysis of individual phases [53]. Scanning electron microscopy creates an image by scanning in consecutive lines. Scanning electron microscopy is capable of creating a high resolution image by using a slow scan speed. Similar to SEM, transmission electron microscopy (TEM) uses electrons to pass through a sample to produce an image. Transmission electron microscopy is beneficial when identifying the phases and crystal structures present in the material and characterizing and identifying defects [53]. A limitation when using TEM is the material must be less than 200 nm thick in order for the electron beam to pass through, so you are only observing a very small portion of the material [53]. Both SEM and TEM are tools used in material analysis on a smaller scale than optical microscopy. Selecting the proper microstructure quantification tool depends on the applications and needs of the user.

1.4.3 Porosity

Porosity is a common defect in AM [47]. The porosity percentage within parts produced through AM is an area of growing interest throughout the AM community since the presence of these pores could cause initiation sites for premature failure events. Finding laser processing parameters for higher density builds is the cornerstone of parameter development in the AM process. In the process of finding acceptable high density processing parameters, former investigations reported five main causes for porosity: insufficient melting, key hole effect, presence of oxides and oxidation, scattering of condensate particles, and

vaporization of low melting point constituents within the alloy [47, 54, 55, 56, 57]. The reasons above are discussed in more detail below.

In general, pores can emerge from five different (or any combination of these) mechanisms: (1) insufficient melting (powder particles trapped inside the pores) which, according to these studies,[47, 54, 55, 56, 57] insufficient melting of powder particles can arise from a mismatch between the layer thickness and the laser track depth, a mismatch between the scanning hatch distance and the laser tracks width, or insufficient laser energy density to generate melting; (2)condensate scattering or over-melting (both melting and vaporization occur, due to laser density, producing recoil pressure and ejecting material over the rest of the components); (3) key hole effect (onset of vaporization gas trapped in melt pool); (4) presence of oxides (largely material dependent, the more sensitive to oxygen levels the material is, the more susceptible the process is to oxidation-based pores); (5) vaporization of low melting point constituents (when the laser beam melts the powdered material, if the temperature of the beam reached the vaporization temperature of a constituent in the material, it will vaporize, leaving porosity behind). In order to avoid these mechanisms, choose an acceptable scanning strategy, ensure suitable laser track width and depth with respect to the layer thickness, and ensure the process is conducted in a pure melting region to avoid defects due to vaporization [58, 59].

Since porosity is a common defect that weakens AM materials, a further investigation of its effects on the subsequent mechanical behavior needs to be understood. Therefore, this study focuses on the effect of porosity on the mechanical behavior at different strain rates. Further detail about porosity is discussed in Chapter 2.

Chapter 2

Porosity Effect on the Mechanical Behavior

This chapter will provide some insight from previous studies that have quantified and examined the effects of porosity on the mechanical behavior of various materials. An overview of past work helped determine research gaps that were discovered and sought-out in this study. Similarities with these studies and this work will be pointed out in order to justify that the methods chosen are well accepted.

2.1 The Effect of Porosity

From the mechanics of materials perspective, porosity could deteriorate the mechanical behavior of AM parts and leads to catastrophic. Therefore, several investigations on the effect of porosity on multiple different materials under various loading conditions has been conducted in order to determine the cause and impact of porosity. Through various studies, it has been widely accepted, that the lower the porosity percentage, the smaller the possibility of the part failing under these types of loading. However, there should be a length scale and size and frequency threshold below which the effect of porosity is inconsequential. Quantifying such thresholds is critical in determining performance and life expectancy of components, which also have substantial economic consequences. Findings from these studies are briefly discussed as follows.

2.1.1 Porosity Effect on the Mechanical Properties of Titanium

Ti is comparable in strength to steel, but has a lower density. Ti is used in several aerospace and industrial applications because of its high strength, relatively low density, and resistance to corrosion [60]. Since it is widely used, several studies have been conducted to quantify the effect of porosity on the mechanical properties of AM Ti. Gong et al. studied the mechanical properties of Ti-6Al-4(vanadium)V that were AM by SLM and electron beam melting (EBM) at various combinations of processing parameters to observe the effect of different power densities on the mechanical properties [61]. The samples in this study were conducted on the as-built (AB) samples only. Optical microscopy and scanning electron microscopy (SEM) was used to observe the amount of porosity in the samples to correlate the failure mechanisms to the underlining amount of porosity. Gong et al. determined defects in a SLM and EBM AM process in Ti-6Al-4V alloy degrade the mechanical properties

even when the defects are in amounts of only 1 vol.% [61]. Furthermore, when these defects occurred in amounts up to 5 vol.%, the mechanical properties typically end up being unacceptable because the large amount of porosity will cause premature failure (fracture, buckling, lower stress, lower strain, etc.) of the part [61].

Yavari et al. studied the macroscopic properties of SLM Ti-6Al-4V meta-material at three different topologies (the geometric properties and spatial relations of the sample) [62]. This study quantified porosity through SEM and X-ray CT scanning. Static and fatigue testing was conducted on a INSTRON and a MTS machine. It was observed that both the quasi-static and fatigue properties are highly topology dependent as well as on porosity. It was also observed that porosity negatively influenced the relationship between the alternating stress versus the number of cycles to failure (from over 1×10^6 to 1.5×10^5) [62]. They showed higher porosity levels resulted in shorter fatigue lives for constant levels of stress applied on the samples [62].

Biswas et al. investigated Ti-6Al-4V alloy under uniaxial static and dynamic compression loadings at three different porosity levels [3]. The quasi-static tests were conducted on an MTS machine and the dynamic tests were conducted on a split-Hopkinson (kolsky) bar. In addition to quantifying the porosity, SEM and EBSD analyses was conducted to study the failure mechanisms. Figure 2.1 demonstrates the effect of porosity at 0, 10, and 20% porosity levels. Figure 2.1 shows that for the Ti-6Al-4V samples with larger porosity amounts, the strain in general increases with the increased porosity due to the increased compliance for the 10% and 20% porosities. Figure 2.1 also shows that the 10% porous material has a reduced amount of ductility than the 0% porous material while the ductility of 20% porous material appears to be comparable to the 0% porous structure, i.e., did not exhibit appreciable increase of ductility. [3].
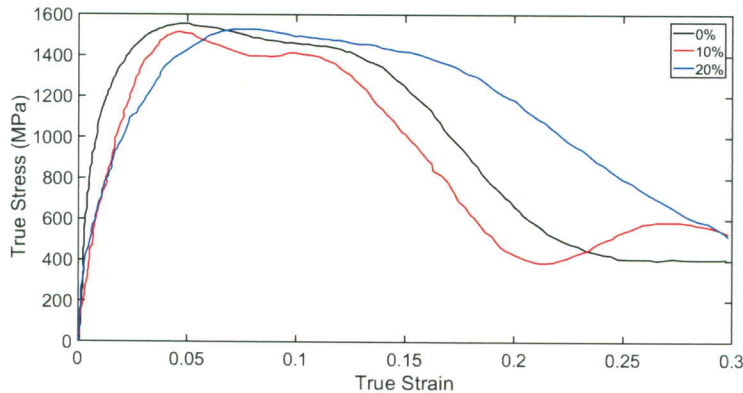
Figure 2.1: The engineering stress–strain curves representing the dynamic compression behavior at a strain rate of 8×10^3 of Ti-6Al-4V with 0, 10, and 20% original porosity. [3]

2.1.2 Porosity Effect on the Mechanical Properties of Steel

Steel is an iron-carbon alloy that exhibits exceptional mechanical strength, ductility, and responsive to heat treatment, making steel irrepressible. Because of this, it is widely used in infrastructure, tools, ships, weapons, and appliances [63]. Since steel is an attractive material, several studies quantifying the effects of porosity on the mechanical properties under various loading. Carlton et al. revealed that the SLM process constructs metals with a wide range of various porosity distributions [64]. The team's overall observation was AM stainless steel built with low porosity showed fracture mechanisms similar to wrought

samples, while AM stainless steel built with an assorted pore distribution exhibited a flaw driven failure. Also displayed, other than solely only bulk density, pore size and morphology are also highly important when evaluating an AM metal's mechanical properties [64].

Kurgan observed the microstructure and mechanical behavior of AM AISI 316L stainless steel as a function of the amount of porosity in the samples [65]. In the study, porosity was quantified by light optical microscopy. The samples were mechanically tested under tension, fatigue, and hardness. Kurgan concluded that an increase in porosity resulted in a decrease in the hardness, fatigue strength, and tensile strength. Also concluded was the sintering temperature, time, and atmosphere (i.e. air or other gases used in the process) are important parameters in decreasing the porosity in the AM powder metallurgy process [65].

2.1.3   Porosity Effect on the Mechanical Properties of Copper

Cu is a common element in alloys to increase the alloys thermal and electrical conductivity so the material can be used in high temperature environments. Zhang et al. studied the quasi-static (QS) compression behavior of AM porous Cu of low to medium (5.9 - 55.5%). In the study, a servo-hydraulic testing machine was used to compress the samples. The porosity size and frequency was measured through SEM and found that two different pore sizes existed within the Cu samples: macro-(200-500μm), and micro-(10 - 20μm) porosity. Figure 2.2 describes the QS compression results from Zhang's study. It can be observed that as porosity increases, the mechanical strength decreases by 75% but the elongation increases by 81% due to the sample acting more like a porus structure rather than a bulk structure. [4].
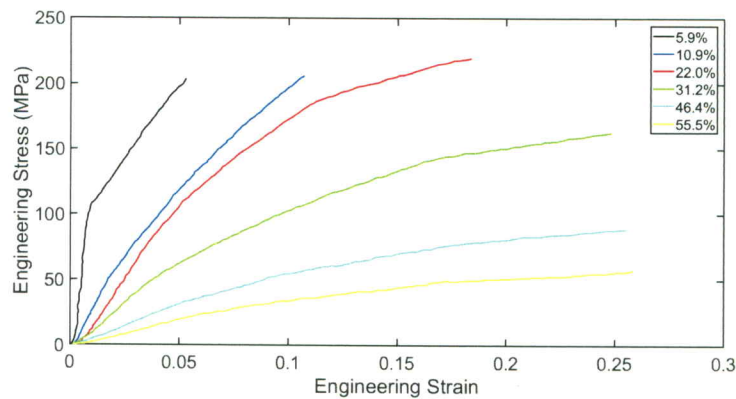
Figure 2.2: The engineering stress–strain curves representing the quai-static compression behavior of porous Cu with 5.9–55.5% original porosity. [4]

Li et al. studied the microstructure and the influence of porosity on the mechanical properties of Cu-35Ni-15Al alloy in cast and porous states [5]. In this study, the porosity distribution and microstructure was determined by using SEM. This study's results show that the yield strength of porous alloys increases continuously with decreasing porosity as shown in Figure 2.3 [5]. From Figure 2.3, it can be seen that as the porosity increases within the material, the yield strength decreases by 50%.
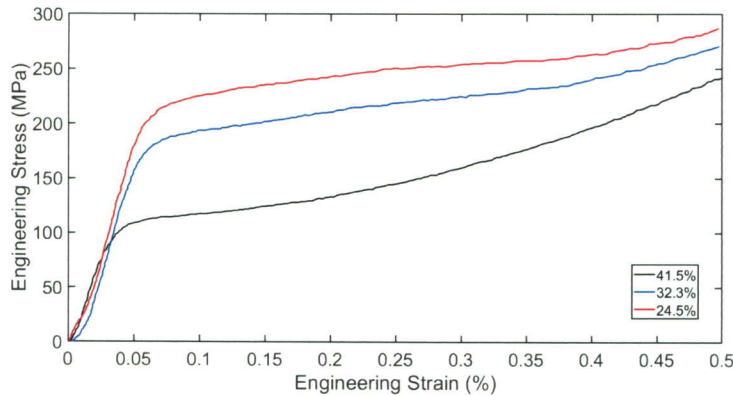
Figure 2.3: Engineering stress vs engineering strain plot for Cu-35Ni-15Al alloy at 24.5%, 32.2%, and 41.5% porosity in the sample [5]

2.1.4 Porosity Effect on the Mechanical Properties of Magnesium

Magnesium increases the mechanical, fabrication and welding characteristics of metals when used as an alloying element which are useful in airplane and automobile industries [66]. Mayer et al. also observed the effect of porosity on the fatigue properties of magnesium and Al alloys [67]. This study utilized SEM to observe the crack initiation location to determine the size and distribution of porosity at that location. It was shown that in almost all of the fatigue samples, the failure was due to porosity acting as crack initiation points in the material [67].

Gangireddy et al. investigated the microstructure and dynamic behavior of an AM magnesium alloy, WE-43, at various processing parameters at both AB and hot isostatically pressed (HIP) conditions [68]. The porosity distribution was determined by transmission electron microscope (TEM) and the dynamic testing was conducted on a split-Hopkinson pressure bar (kolsky bar). The results show that HIP heat treatment was more effective than AB at higher initial porosities but was not able to improve significantly due to the enclosed nature of the pores. Also, strength is dependent on the amount of porosity accumulated in the sample [68].

2.1.5 Porosity Effect on the Mechanical Properties of Inconel 718

Trosch et al. studied the effect of the AM SLM process on the microstructure and tensile properties of IN718 (which is a high-strength, corrosion-resistant, Ni-Cr superalloy) at room and elevated temperatures (450°C and 650°C) and compared the results with TM methods, forged and cast IN718 [69]. It was found that the SLM process induces a frequent amount of porosity within the samples. Torsch and the team quantified the microstructure and porosity through SEM and optical microscopy. Through the study, it was concluded that the AB SLM IN718 samples have a higher porosity size (around 0.075%) and frequency compared to forged and cast IN718, resulting in a reduction in mechanical properties of 970-1050 MPa. Furthermore, it was found that after a HIPed heat treatment, the porosity percentage reduced to 0.02%, which is comparable to forged IN718, and highly surpasses the cast IN718 samples that have a 0.2% porosity percentage. Lastly, the SLM IN718 samples were superior to the forged and cast IN718 samples at room temperature and 450°C [69].

Sangid et al. studied the role of heat treatment and build direction on the microstructure and mechanical properties on SLM IN718 [70]. The SLM process created a large concentration of porosity at the surface of the AB samples which was viewed through X-ray

13

microcomputed tomography. After monotonic and cyclic loading, the microstructual deformation mechanisms are quantified through digital imaging correlation, and the AB and post-processing mechanical properties are compared with respect to the build direction. It was concluded that post-processing significantly reduces the amount of porosity from a pore size of 3.25 to 1.5 μm within the sample compared to AB samples, but the majority of pores were still located near the surface. It was also found that the AB tensile properties are significantly anisotropic due to the grain morphology from the laser path during the SLM process, but, post-processing reduces the anisotropy and the strength significantly increases due to a refined microstructure and a reduction in porosity [70].

Aydinoz et al. studies the effect of porosity on the monotonic and low cycle fatigue behavior of SLM IN718 at different heat treatment conditions and the effect the heat treatment has on the microstructure [6]. Porosity was quantified through X-ray micro-computed tomography and was found that the majority of the pores were located at the surface and was calculated to be 0.1% of the volume. After the HIPed heat treatment, recrystallization caused significant changes to the microstructure and a reduction in porosity. It was observed that the SLM process led to a columnar grained microstructure in the as built samples, and equiaxed grains after HIPing. Figure 2.4 shows the tensile behavior of the SLM IN718 samples at the AB, HIPed, and SA heat treatments. It was observed that a decrease in yield strength with an increase in elongation at failure of SA and HIP processing. The strange behavior can be attributed to the microstructure. The AB samples have a higher yield strength and low ductility due to sub-micron cell structures and high dislocation density, while the SA samples have a lower yield strength than the AB samples due to a decrease of the dislocation density but the yield strength remains higher than the HIPed samples due to conservation of the sub-micron cell structures which act as barriers for dislocations under monotonic loading [6].
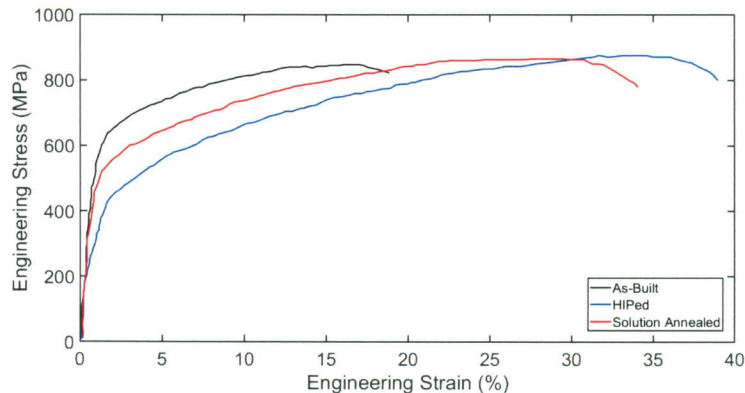
Figure 2.4: The engineering stress–strain curves representing the tension behavior of SLM IN718 as a function of AB, HIPed, and SA heat treatments [6]

.

These studies have conducted similar procedures as preformed in this study such as the AM process (SLM), quasi-static tension and compression loading, comparing the porosity effect of mechanical properties of post-processing heat treatments, quantifying porosity by X-ray computed tomography, and utilizing measurements from digital imaging correlation. However, a direct correlation between the amount of the porosity and the state of stress (e.g., tension, compression) or rate of the deformation (e.g., quasi-static, dynamic) should be made. Such a correlation will provide new insights regarding the allowable amount of porosity in AM parts for a specific loading condition, leading to cost savings by eliminating

unnecessary post processing, e.g., inessential further heat treatments. This study aims to bridge the gap between the direct effect of porosity and the mechanical strength and behavior under low and high-strain rate deformation of AM parts made from a Nickel(Ni) based super alloy (IN718) in bulk and LS.

Chapter 3

Material, Processing, and Heat Treatment

This chapter will discuss in detail the selected material, the AM material processing, as well as the post processing heat treatment procedures that is applied to the samples in this study. Each sample was AM at NASA Marshall Space Flight Center, and further details on the specifics are discussed in Section 3.2.1 and Section 3.2.2. The first section will discern what makes this material desirable and the building blocks that make the material superb. Then, a deep-dive into the AM material processing and heat treatment that occurs to amplify the mechanical properties of the AM IN718 samples. Finally, the specific machines and heat treatments that were used on the bulk and LS will be discussed.

3.1 Rational for Investigating AM Inconel 718: Specifications and Mechanical Properties

IN718 is a Ni-Cr based superalloy used extensively in applications that require high strength at extreme temperatures. It associates good creep and rupture strength with a high resistance to fatigue. It possesses long time strength and toughness up to 700°C along with superb corrosion resistance. Due to these excellent mechanical properties at such high temperatures, IN718 is of particular interest to nuclear and aerospace industries. The wide range of environments in these critical applications points towards a need for exceptional mechanical properties under extreme environments. When comparing the mechanical properties at high temperatures to other metals such as steel and magnesium, IN718 dominates as shown in Figure 3.1. It is also superior when compared to other superalloys [71]. To understand the mechanism for the powerful mechanical properties, it is necessary to discern key elements in IN718 as shown in Table 3.1 [72]. The IN718 samples have chemical composition corresponding to UNS N07718, AMS 5662, AMS 5664, W.Nr 2.4668, and DIN NiCr19Fe19NbMo3 standards. Each element and their role is described below [8]:

- Iron(Fe) coupled with a low Ni content lowers the price

- Atoms of Fe, Cr, Mo and Nb can substitute to Ni within the metallic matrix to create solid solution hardening and hardening by a precipitation of ordered inter-metallic phases, γ' and γ'' are combined to strengthen he material

- Ti and Al form by precipitation into the inter-metallic phase γ', Ni3(Ti, Al), hardened

16

by solid solution of Nb and Ti at room temperature and of Tungsten or Mo at high temperature

- At around 650°C, Nb couples to Ni to form by precipitation of the γ'' phase (Ni3Nb), which is the primary strengthening agent, which has superb mechanical properties at low and moderately high temperatures

- The next structural components are primary carbides (created by elements such as Cr and Ti) and secondary carbides (created by elements such as Cr, Cobalt, Mo and Tungsten)

Table 3.1: Limiting Chemical Composition

Material	Chemical Composition, %
Nickel (plus Cobalt)	50-55
Chromium	17-21
Iron	Balance
Niobium (plus Tantalum)	4.75-5.5
Molybdenum	2.8-3.3
Titanium	0.65-1.15
Aluminum	0.2-0.8
Cobalt	1 max
Carbon	0.08 max
Manganese	0.35 max
Silicon	0.35 max
Phosphorus	0.015 max
Sulfer	0.015 max
Boron	0.006 max
Copper	0.03 max
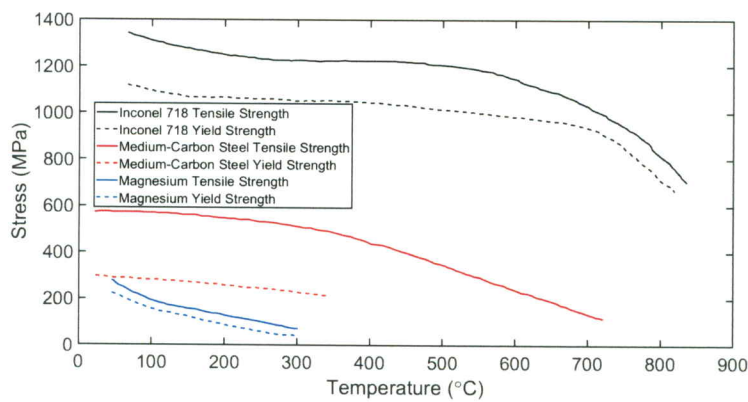
Figure 3.1: Comparing the stress vs temperature properties for IN718, medium-carbon steel, and magnesium [7, 8, 9]

.

17

3.2   Material Processing and Heat Treatment

In order to show the effect of porosity on the quasi-static and dynamic properties of IN718, two types of sample geometries were configured and tested. First, a traditional bulk solid sample was tested in order to understand the porosity effect on the parent material before testing the complex lattice structures. After an understanding of the of porosity at different heat treatments on IN718, a further investigation into the effects of lattice structures was conducted.

The samples were made of IN718 by using a Powder Bed Fusion (PBF) process called selective laser melting (SLM) at the Marshall Space Flight Center (MSFC) to an accuracy of $\pm 40 - 60 \mu m$ powder particle size distribution and spherical morphology. A step-by-step process of the SLM procedure was as follows: (1) a 0.2mm thick layer of material was spread across the build plate; (2) a laser outlines the first layer of the structure, melting the powder to form a solid layer; (3) The build plate lowers and a new layer of powder was spread across the previous layer; (4) The next layer of the structure is outlined and fused together with the previous layer; (5) This process was repeated until the entire structure was created. The unused powder is deposited back into the AM machine for further use. The loose powder not fused to the sample was removed in the post processing procedures. To explore the direct effect of porosity on the quasi-static and dynamic behavior, AB samples were subjected to post-processing heat treatments, which in turn, leads to different porosity size and frequency as presented in Section 4.1. During the AM SLM process, there is a large temperature gradient from the bottom layer to the top layer. The bottom layer is already cool while the top layer is still hot causing internal stresses in the sample. In order to mitigate the internal stresses, the Stress Relief (SR) procedure is applied. It is reported that the SR process removes these internal stresses. Oak Ridge National Laboratory and NASA Langley Research Center conducted a study on AM IN718 turbine blades to determine if residual strains could be measured in components with internal structures [73]. Their team concluded that after a thorough SR heat treatment, residual strains become more uniform throughout structure, suggesting that the product will be less likely to distort during service [73]. The SR heat treatment is intended to account for the issues outlined in Section 1.4.1. The next stage of heat treatment is HIP. This process applies pressure to the sample while under a high temperature. This allows the porosity inside the material to minimize. Surface defects causing pores, internal pores, and internal cracks are a problem for post-processing heat treatments because they allow deeper infiltration into the material from air during high heat cycles, and cause pre-mature failure, but, these defects may be closed by HIP, as has been shown in SLM Ni-based superalloy parts [74].

It is known throughout the literature that IN718 is hardened by the precipitation of the γ' and γ'' phases into the matrix of the metal generated through heat treatments [8, 72]. The aging elements (Ti, Ni, Al) must dissolve in the metal matrix for this metallurgical reaction to adequately take place [72]. In order for this process to occur, the IN718 samples need to be solution heat treated then precipitation (age) hardened (SA), which is the final heat treatment used in this study. The SA temperature was selected above the solvus temperature at which all undesired phases dissolved, similarly, the time was selected to be long enough to dissolve the precipitates but short enough to limit grain growth. The parameters for each heat treatment are determined from the Ni-Cr phase diagram. The Ni-Cr phase diagram reveals that the melting point of Ni and Cr at atmospheric pressure is 1455°C and 1907°C, respectively. Ni-Cr has a eutectic region, where the face-centered cubic (FCC) Ni and body-centered cubic (BCC) Cr are formed, occurring at 51% Cr at 1345°C [75].

3.2.1 Bulk Sample Processing and Heat Treatment

The IN718 bulk samples were made on a Concept Laser M1 AM Machine. A detailed list of the heat treatment processes as well as the typical mechanical properties for AM IN718 are presented in Table 3.2. The average polished quasi-static (QS) sample dimensions for compression were $9.96 \times 5.95 \times 5.95$ mm^3 and the tension samples (gauge section) were $25.2 \times 1.95 \times 7.95$ mm^3 and the CAD model of the samples that were sent to NASA are shown in Figure 3.2a. The average polished dynamics sample dimensions for compression were $6.80 \times 4.94 \times 4.95$ mm^3 and the tension samples (gauge section) were $9.96 \times 1.92 \times 5.94$ mm^3 and the corresponding CAD model is shown in Figure 3.2b. An image of the printed samples are shown in Figure 3.3 and 3.4. Figure 3.4 shows the samples still on the build plate right after the AM process. After the AM process and the samples were built, a wire electrical discharge machine (EDM) was used to cut the samples off the build plate. Table 3.3 shows the overall number of samples tested for one set of mechanical loading (i.e. quasi-static). The same amount of samples were tested dynamically as well. The table also depicts the samples that were computed tomography scanned (these were the dynamic tension samples).

For all the bulk samples, the properties of the AB samples are compared with SR, and HIP conditions. The SR process was conducted at 1065°C ±13°C for 1.5 hour -5/+15 min, in an argon atmosphere and the HIP procedure was performed at 1163°C ±13°C for 4 hours at 102 MPa. Heat treatments were performed in the order of SR, then HIP. For example, a HIP sample undergoes both SR and HIP heat treatments.

Table 3.2: Physical Properties of Post Processing Heat Treatments in bulk AM IN718

Typical Physical Properties			
Mechanical Properties	DMLS As Built	DMLS SR*	DMLS HIP'ed*
Tensile Strength	875 MPa	917 MPa	1275 MPa
0.02% Yield Strength	772 MPa	517 MPa	930 MPa
Modulus	179 GPa	193 GPa	200 GPa
Elongation	30%	42%	24%

DMLS - Direct Metal Laser Sintering

*SR - Stress Relief, 1065°C for 1.5 hour

*HIP'ed - Hot Isostatic Press, 1163°C for 240 min at 102 MPa
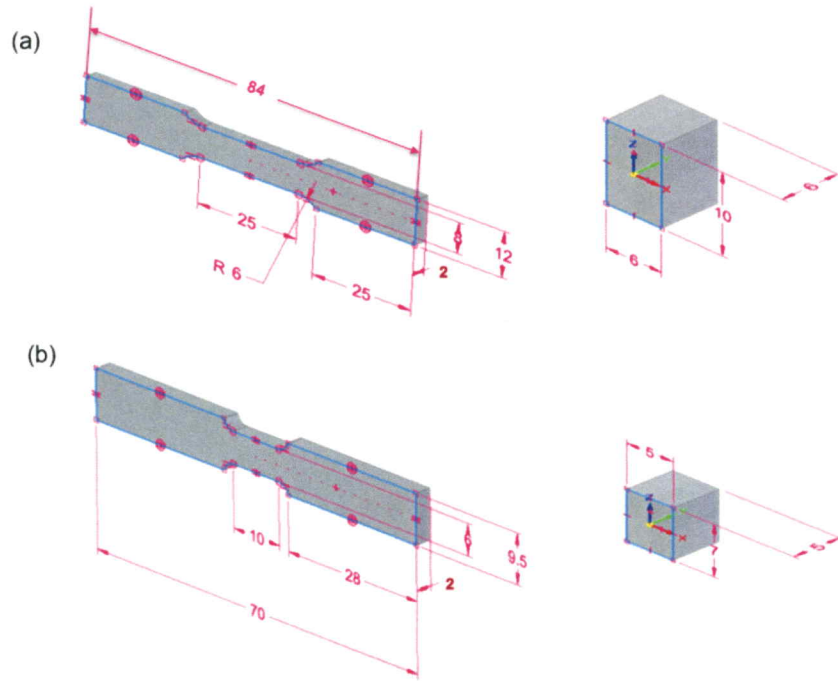
Figure 3.2: The (a) quasi-static and (b) dynamic tension and compression CAD models with their corresponding dimensions that were sent to NASA and uploaded into the AM machine

Figure 3.3: The AM bulk tension and compression samples used for quasi static (left) and dynamic (right) testing
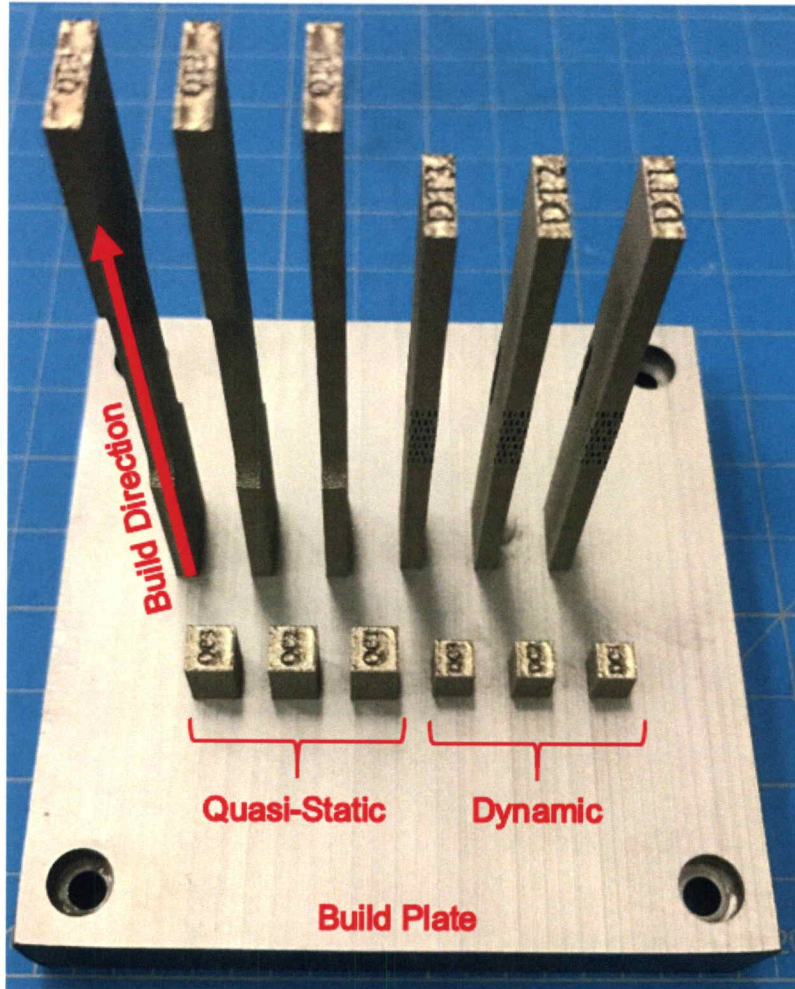
Figure 3.4: The AM bulk tension and compression samples used for quasi static (left) and dynamic (right) testing

Table 3.3: Overall number of bulk samples evaluated with respect to heat treatment

	Tension	Compression
AB	2*	2
SR	2*	2
HIPed	2*	2

* indicates one separate sample was
computed tomography scanned

3.2.2 Lattice Structure Processing and Heat Treatment

LS were made of inert gas atomized carpenter IN718 powder on a EOS 290 AM machine. The details of the laser parameters and scan strategy are outlined in Table 3.4.

Table 3.4: Material, laser parameters, and scan strategy used in the manufacture of AM IN718 LS.

Material	Inconel 718
Core laser power (W)	285
Core scan speed (mm/s)	960
Outside counter laser power (W)	90
Outside counter scan speed (mm/s)	900
Inside counter laser power (W)	138
Inside counter scan speed (mm/s)	390
Hatch width (mm)	0.11
Bild layer thickness (mm)	0.04
Scan path	Islands
Support laser power (W)	100
Support scan speed (mm/s)	900
Beam comp (mm)	0.015

LS with four different building unit cell topologies and two different unit cell size were manufactured. Similar to the bulk sample, after the AM process and the samples were built, a wire electrical discharge machine (EDM) was used to cut the samples off the build plate. The build topologies and their relative densities are shown in Figure 3.5. In this study a unit cell refers to the smallest structural element that repeats periodically in a three dimensional configuration to build the LS, also shown in Figure 3.5. Samples are named conforming to their building unit cell topology. The relative density for the manufactured samples were calculated to be octet truss (OT), 30%, rhombic dodecahedron (RD), 20%, diamond (D), 20%, and dode-medium (DM), 15%. The physical polished dimensions of the cubic samples with 2 mm and 4 mm unit cell size were $9.95 \times 9.95 \times 9.60$ mm^3 and $15.75 \times 15.75 \times 15.25$ mm^3. Table 3.5 shows the overall number of samples that were mechanically tested and also the samples that were computed tomography scanned(CT) and used for microstructure. Quasi-static loading experiments were conducted on both 2 mm and 4 mm unit cell size samples, while dynamic loading was only conducted on samples with 2 mm unit cell size because of experimental hardware constraints.

Similar to the bulk sample, the LS properties of the AB samples were compared to the SR, HIP, and SA heat treatment conditions. The SR process was preformed at 1065°C ±13°C for 1.5 hour -5/+15 min in an argon atmosphere, the HIP process was performed at 1163°C ±13°C for 4 hours at 101.7 MPa, while the SA heat treatment procedure was done at 1063°C ±13°C for 3 hours. Heat treatments were performed in the order of first SR, second HIP, third SA. Therefore, a SA sample undergoes SR plus HIP plus SA heat treatments.
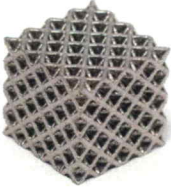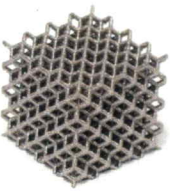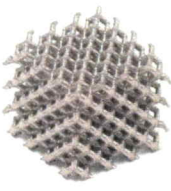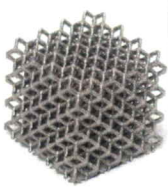
Topology	Octet Truss	Rhombic Dodecahedron	Diamond	Dode-Medium
Build samples using SLM technique				
Relative density (ρ^*)	30%	20%	20%	15%
Building unit cell				
Unit cell size (mm)	2 and 4	2 and 4	2 and 4	2 and 4

Figure 3.5: Geometry, topology, and relative density of the AM LS that were used in this study.

Table 3.5: Overall number of lattice structure samples evaluated with respect to heat treatment, size, and topology

	2 mm Unit Cell Size				4 mm Unit Cell Size			
	AB	SR	HIPed	SA	AB	SR	HIPed	SA
OT	2*	2*	2	2*	2†	2†	2†	2†
RD	2	2	2	2	2	2	2	2
DM	2	2	2	2	2	2	2	2
D	2	2	3	2	2	2	3	2

* indicates one separate sample was computed tomography scanned
† indicates one separate sample was used for microstructure

Chapter 4

Characterization Method

This chapter outlines the different characterization methods utilized in this study. X-ray computed tomography (CT) was used to quantify the amount of porosity in both the bulk and LS. The technical process and parameters utilized in the CT analysis is thoroughly explained. Then, the sample preparation technique of using different grit sand paper to hand polish each sample to take roughly 100 μ off each face of the sample to reduce the large surface voids. This is important so the failure occurs within the material so the material behavior is measured instead of the surface voids causing premature failure. A speckle pattern is airbrushed on the face of interest of the sample in order to measure the displacement of the deforming sample. In order to measure the displacement, digital imaging correlation (DIC) is applied on this speckle pattern to track the speckles during the test. The whole processes is explained in detail below. Finally, the QS and dynamic testing setup is shown and explained in detail. Henceforth, the terms porosity and voids are used interchangeably.

4.1 Porosity Characterization

4.1.1 Bulk Sample Computed Tomography

X-ray CT is a non-destructive imaging technique that produces images of cross-sectional planes through the sample. These images are mathematically reconstructed from a substantial number of two-dimensional projections of the plane of interest in a layer-by-layer manner. The two-dimensional projections are acquired electronically through a linear array of solid-state detectors and an x-ray source that rotates around the part [76]. A physical phenomena that effects the attenuation of the x-ray passing through the material is photoelectric absorption, which solely depends on the atomic number of the material and the x-ray photon energy [77]. Within a CT scan, the x-ray attenuation is measured at a variety of different angles and a cross-sectional reconstructed image is generated which represents the x-ray attenuation in volume elements of the material in a plane perpendicular to the motion of the scan [78]. The CT scanning process provides a description of the solid and void spaces shown in cross-sections through the sample, allowing MATLAB to calculate the porosity volume of each pore within the sample.

The AB, SR, and HIP samples were imaged by a commercial micro CT system, Zeiss Xradia 510 Versa. This CT instrument utilizes a Nordson DAGE transmissive X-ray tube with a tungsten target anode, which operates from 30-160 kV and up to 10 W with a dynamic spot size from 2 to 4 μm FWHM and a maximum 34° cone beam angle. The operational parameters of the X-ray source for this study to obtain sufficient X-ray transmission were

selected at maximum voltage and power, i.e. 160 kV and 10 W. The transmitted X-rays were absorbed by a lens-coupled scintillator with three objectives 0.4X, 4X, and 20X and the visible light imaged by 2.5 x 2.5k CCD with a physical pixel size of 13.5 μm. Based on the required resolution and sample size, 4X was selected to be appropriate without any pixel binning resulting in a 3.5 μm voxel size and $3 \times 3 \times 3$ mm^3 inspection volume after reconstructing the CT data.

The porosity analysis was performed using the imaging process toolbox from MATLAB. The analysis consisted of applying a global threshold value based on the average gray intensity values close to the surface of the material. The binarized data was then processed using morphological operations and filtering based on a 10 μm particle size.

The CT analysis was done to quantify the amount of porosity in each sample and track the changes in porosity in each heat treatment. Both the SR and HIPed heat treatments are meant to reduce the amount of porosity in the sample. These results are discussed further in Section 5.1.

4.1.2 Lattice Structure Computed Tompgraphy

Images for the LS porosity quantification analysis were obtained using a commercial X-ray micro CT Zeiss Xradia 520 Versa system. Materials were imaged with a pixel resolution of 3.37 μm with an accelerating voltage of 160 kV and 15 sec exposure time. The angular step size ranged from 0.15 to 0.2 degrees between the collected scans that equals to 360° per number of projections. The reconstructed tomographic images were processed using an academic version of the commercial software Dragonfly. After analyzing the X-ray images certain detected voids were deleted to avoid erroneous measurements. Voids with a zero aspect ratio were deleted, since a zero aspect ratio means the void is not volumetric. For instance, a void laying in the x-y plane with a zero aspect ratio will not be visible on other planes and will cause misrepresentation of the total void volume if analyzed. The voxel size was approximately 500 μm^3 and voids with a volume less than 10 000 μm^3 were also deleted in order to avoid detection errors due to the scan resolution.

4.2   Sample Preparation

The first step in the preparation process for measuring full-field strain was to polish the faces of interest. For the bulk tension samples, this area is either of the gauge section faces and either one of the transverse faces of the compression samples. For the LS, this area corresponds to one build direction (the face opposite of the build plate), and one transverse direction face. For compression samples, the two faces that were in contact with the compression platens were also lightly polished in order to ensure the two faces are parallel for uniaxial loading. Each face was polished with 320, 600, and 800 grit sand paper. The sample's dimensions were measured before and after polishing for post-processing calculations after. For the bulk samples, the tension samples change in width averaged to be around 90 μm and the thickness around 100 μm. For the compression samples, the change in width averaged to be around 150 μm and the thickness around 153 μm. The LS were similar with the average change in width to be around 110 μm and thickness around 125 μm for the 4 mm unit cell. For the 2 mm, the change in width was around 90 μm and thickness around 95 μm.

A speckle pattern for digital image correlation (DIC) was applied by an airbrush after the sample was polished. A layer of white paint was applied first to the two polished faces.

Then, a fine mist of black paint was used to apply a speckle pattern on top of the white paint. Lubricant was applied to the two faces that were in contact with the compression platens to remove frictional forces between the sample and compression platens making the only force applied on the sample the uniaxial force from the loading machine.

4.3 Digital Imaging Correlation

In order to evaluate the amount of strain on the sample, the non-contact method of DIC was used. For the lattice structures, the interest is to investigate local development of strain, therefore, under compression, strain gauges are not able to accurately measure the local development of strain of the entire sample. As for the strain gauges, they are too bulky for the compression samples and if you decide to use the MTS statistics to measure strain, an error will occur from the machine compliance (machine mechanics, geometry, control system, etc.). DIC therefore can severe as a non-contact measurement to measure the global strain plus is gives the ability to resolve local strain and explain local phenomena.

DIC measures displacement of the speckles from image to image in order to calculate strain and was completed in the VIC2D software by Correlated Solutions. DIC calculates a data point at the center of every subset every stepsize away. For the bulk samples, a subset of 25 pixels with a step size of 12 pixels was used. For the LS, a subset of 24 pixels and a step size of 11 pixels was used for the 4 mm unit cell samples and a subset of 22 pixels and a step size of 10 pixels was used for the 2 mm unit cell samples. Before any load is applied, 5-7 images were taken to measure the fluctuations in the instrumentation. Then, DIC was ran on those images with zero load to see the displacement/strain field. The area of interest (AOI) for DIC was drawn on the first image. The AOI is only applied on the sample (for LS, this excludes the holes). All the data points for each of the images with zero load were taken to get the statistics from them. The standard deviation of that grid data for all the zero load images is what is listed as the uncertainty. Since many of the test parameters were consistent between the experiments (lens, camera, exposure time), the uncertainties are similar so an average value of all the tests were taken and is what is recorded. Given the resolution of the camera and the sample dimension, the strain uncertainty for the bulk samples was approximately 480 microstrain in compression and 600 microstrain in tension. Strain uncertainty in the 2 mm samples was approximately 240 microstrain and the 4 mm samples was approximately 1000 microstrain.

Figure 4.1-4.3 illustrates the DIC strain map projected onto the speckled samples. As the load is applied, the strain map varies according to the strain on the entire face of the sample. Since it is assumed the samples are isotropic, this strain map represents the response of the entire sample. Figure

eyy[%]

0.00

39.9

66.6

86.8

106.5

$\varepsilon_1 = 0.00$　　$\varepsilon_2 = 0.22$　　$\varepsilon_3 = 0.26$
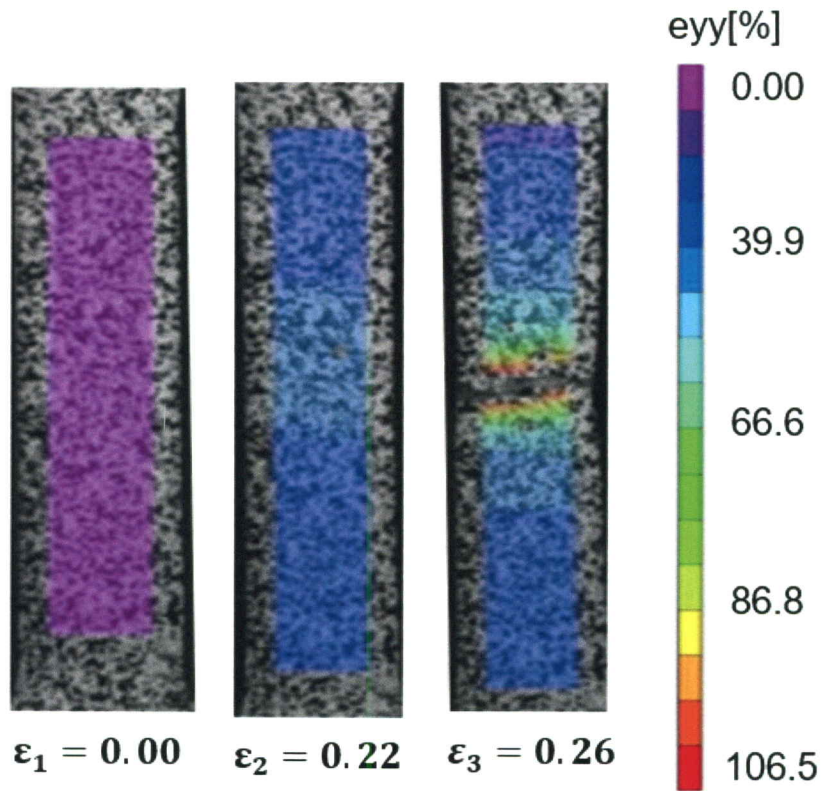
Figure 4.1: A speckled quasi-static tension sample overlaid with the DIC strain map at three different instances during testing. The corresponding strain value in the y-direction is below each image. The scale bar to the right displays the strain percentage in the y-direction.
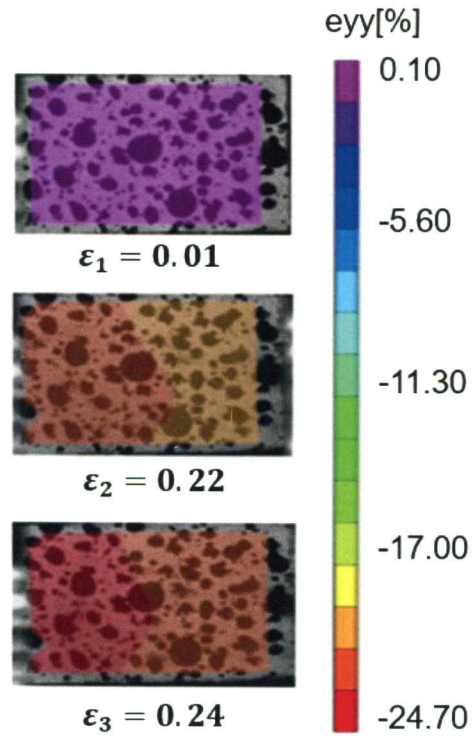
Figure 4.2: A speckled dynamic compression sample overlaid with the DIC strain map at three different instances during testing. The corresponding strain value in the y-direction is below each image. The scale bar to the right displays the strain percentage in the y-direction.
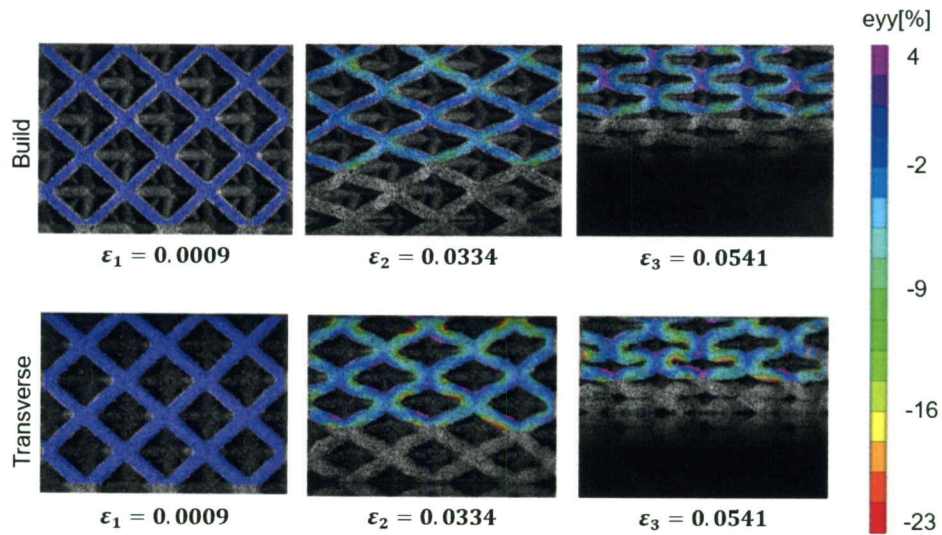
Figure 4.3: A speckled OT lattice sample overlaid with the DIC strain map at three different instances during testing. The corresponding strain value in the y-direction is below each image. The scale bar to the right displays the strain percentage in the y-direction.

4.4   Quasi-Static Testing

QS tests were preformed on a Materials Testing System (MTS) machine (Model 661.20F-03) that has a maximum capacity 100 kN. The test ran until the sample reached a failure point (before the test started, the failure point of the material was defined to be when the sample fractured or the desired deformation was reached) then, the test was manually stopped. Point Grey Grasshopper cameras (GS3-U3-51S5) monitored the deformations of each sample that was set up perpendicular to the speckled surface as shown in Figure 4.4. This camera has a resolution of 2448 × 2048, 75 FPS, 5 Megapixels, and a 3.45 micrometer pixel size. The image acquisition rate was set to be one frame per second for both bulk and LS. The cameras were set up perpendicular to the surfaces of interest. If the camera is not perpendicular, the right and left side of the images will be out of focus while the center of the image is in focus causing the DIC to drop the AOI when the load is applied. A Cole-Parmer 41500-50 fiber optic illuminator with a 150 W halogen bulb was used to illuminate the samples illustrated in Figure 4.4. Without the light, when the compression testing starts, the sample will be too dark for VIC2D to pick up the image. Additionally, if there is too much light, this area of the sample will be over saturated and will be dropped in the analysis. The light distribution is checked through a software called Vic Snap (also by Correlated Solutions). Vic Snap is also the software used to be the interface between the user and the test to take images. For each test, the deformation rate was one millimeter per minute resulting in an approximate strain rate of $\approx 10^{-3}$ s^{-1}. For the compression tests, a M27x2mm fixed and spherical head compression platen (shown in Figure 4.4) was threaded onto the MTS machine. Since the top platen is a spherical head, this allows for the load to be uniaxial while the sample is deforming. Before the compression test started, lubricant is applied to the sides of the sample in contact with the compression platens. This was done to remove friction between the sample and the platens so only a compressive load is applied. For the tension tests, the compression platens were removed and tension grips were threaded on.
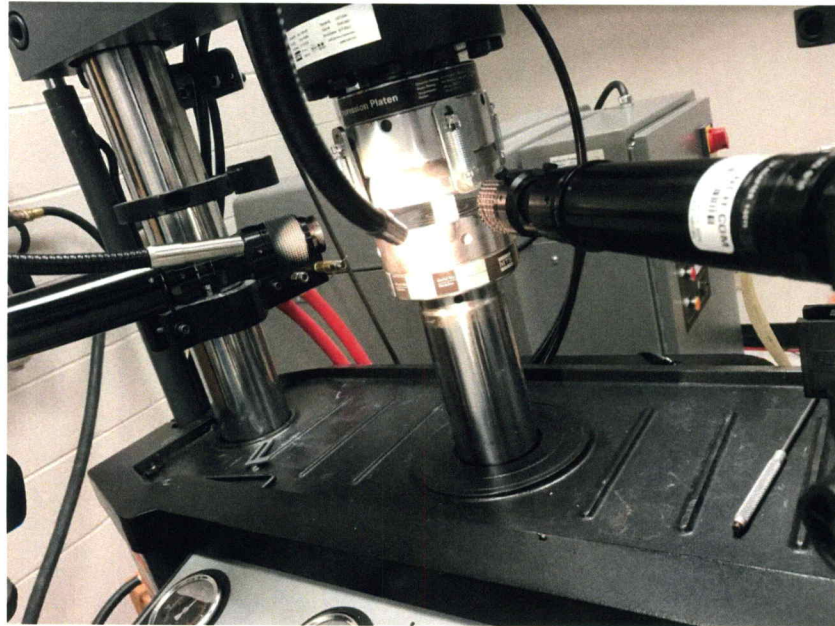
Figure 4.4: MTS test setup of the 4mm unit cell size OT LS compression test.

4.5 Dynamic Testing

Dynamic testing was conducted using a split-Hopkinson Pressure bar (Kolsky bar) at the strain rate of $10^3 s^{-1}$. The Kolsky bar setup for these experiments is shown in Figure 4.5. The Kolsky bar consists of two bars: an incident (input) and transmission (output) bar. These bars are maraging steel having a diameter of 19 mm. The samples were placed between the two bars. The opposite face of the incident bar not in contact with the sample is impacted by a 610 mm striker bar. The gas chamber is pressurized by air to 100 psi that houses the striker bar. The striker bar creates a compressive pulse that propagates through the incident bar to the sample. Once this compressive pulse reaches the sample—incident bar interface, multiple reverberations transpire within the sample. A pulse then propagates through the transmission bar while a reflected pulse is returned to the incident bar. A momentum trap (shown in Figure 4.6) was placed on the incident bar to ensure that the sample is loaded only once instead of a repeated load. This is important so the initial, single pulse is observed because after the first pulse, the sample deforms into the plastic regime so the measurements after the first pulse are not useful for this experiment. Therefore, the failure point for the dynamic tests was defined to be the condition of the sample after the first pulse. Two strain gauges are used (one on the incident bar and one on the transmission bar) 914 mm away from the sample-bar interfaces for measuring the incident pulse, the reflected pulse, and the transmitted pulse. For both the incident and transmission bar, one end is threaded while the opposite end is not. For the compression tests, inserts also made of maraging steel was placed between the two bars to prevent damaging the bars and the samples are placed in between. For the tension tests, the transmission bar was turned around so both threaded ends of the bars are facing each other. Then, the tension grips are threaded onto each bar. An ultra high-speed imaging Shimadzu HPV2 Camera having 1,000,000 frames per second at 312×260 pixel resolution and a Phantom v2511 having 110,000 frames per second at 512 x 320 pixel resolution was used during testing. A SURE-Bright Fixed Focus LED light was used to illuminate the sample.
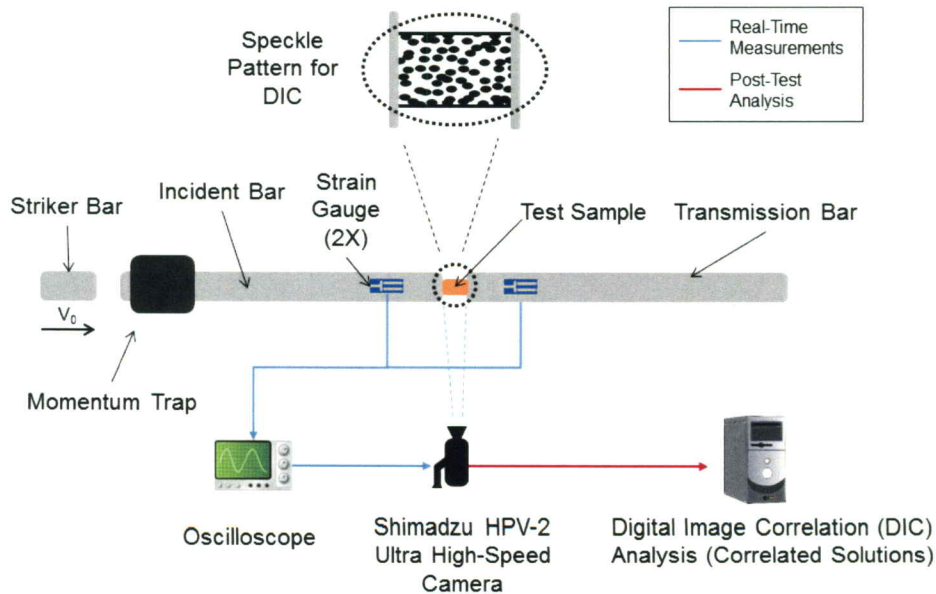
Figure 4.5: Schematic on the Kolsky bar setup outlining each component and their relative placement used during the dynamic testing.

31
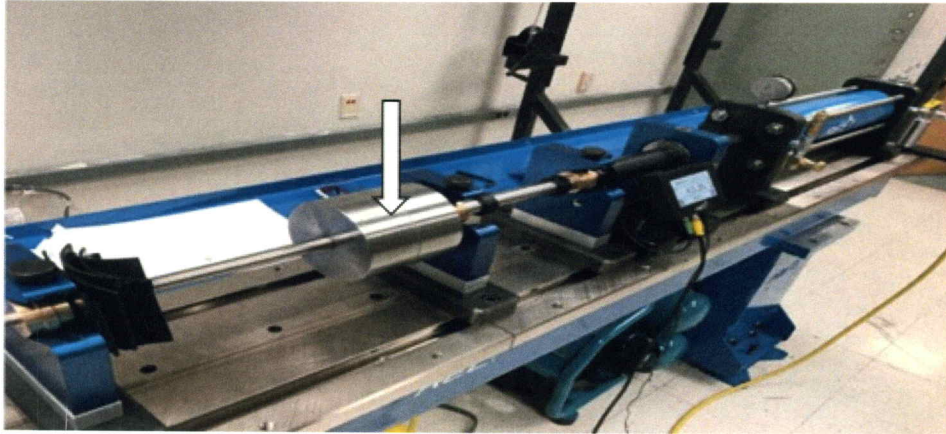
Figure 4.6: The Kolsky bar used during the dynamic testing for both bulk and LS samples pointing out the momentum trap.

Chapter 5

Bulk Samples

This chapter outlines the results from the X-ray CT and mechanical testing of the AM IN718 bulk samples. A thorough discussion followed by the results are presented. The CT analysis is explained in detail which gives the ability to track the evolution of porosity throughout the sample. Following the CT analysis is the results from the QS and dynamic testing. The CT analysis was presented before the QS and dynamic results in order to try to establish a relationship between the failure mechanisms and the corresponding porosity distribution.

5.1 X-ray Computed Tomography

A volumetric X-ray CT investigation was conducted on the QS tension samples at AB, SR, and HIPed heat treatment conditions to quantify the amount of porosity within the samples. Table 5.1 outlines the total amount of porosity that was calculated for each heat treatment. The total number of voids decreased by 44% from AB to SR and 94% from SR to HIPed. From this analysis, it can be seen that HIPing has a bigger influence on porosity reduction than SR. Similarly, the void volume ratio calculated, which represents the total porosity volume divided by the total volume of the space analysed, decreased during SR and HIPed heat treatment.

Table 5.1: Overall number of detected voids from the image analysis on X-ray scans for quasi static tension samples

Heat treatment	Total analyzed volume (μm^3)	Total number of voids	Total void volume ratio %
As Built	62,713,098,381	957	0.0148
Stress Relieved	63,068,846,983	533	0.0104
HIPed	61,631,130,874	27	0.0003

Figure 5.1 shows three arbitrary planes, noted as P0, P1, and P2 in the image, from the CT scan analysis for AB, SR, and HIPed QS tension samples in order to visualize and quantify the void distribution. For any given plane, it is expected that porosity will reduce after heat treatment. On the contrary, it is shown from Figure 5.1 the SR has raised the number of voids in the P2 plane. This is an interesting discovery because the amount of porosity is expected to decrease as further heat treatment is applied to the sample, especially not increase porosity. This unusual phenomenon could be attributed to the heat treatment process causing the surface roughness to be increased, creating deep pockets on the surface, which are then corrected with the HIPed heat treatment because of the applied pressure, or it could be from not being able to control the sample preparation sanding to

a fine tolerance. On the other hand, the amount of porosity decreased when subjected to HIPed heat treatment (Figure 5.1). The size distribution and fraction of voids decreased through the progression of each heat treatment. Figure 5.2 demonstrates frequency and size distribution of the porosity as a function of three different heat treatments noted in the picture.

An analysis on the effect of the heat treatment on the area fraction of the voids are presented in Figure 5.3. The area fraction for all the CT image slices, which covers the entire gauge section of the sample, are considered in the analysis. The top graphic in Figure 5.3 illustrates the area of interest and a visualization of how the CT analysis slices were taken normal to the build direction. From Figure 5.3 it can be seen that the HIPed heat treatment has removed almost all the voids, but, when it comes to the SR heat treatment, the void area fraction (VAF) decreases for the first 50 slices and for the last 30 slices VAF increases unexpectedly. Most of the voids are located on the surfaces of each sample. This trend stayed consistent throughout each heat treatment. This phenomenon could be attributed from the scan path of the laser during the AM process. Visualizing a 2D build plate of raw material powder, for these samples, the laser starts in one of the corners of the sample an moves horizontally towards the opposite edge. Once the laser approaches the edge of the sample, it drops down vertically in a half-circle and continues in the opposite direction that it originally was going. This process continues until the entire sample layer has been passed over. Then the laser will trace the outer layer of the sample before moving onto the next layer. Since the laser drops down in a half-circle instead of a straight line, when the final laser pass traces the sample, that leaves small areas between the curved edges of each laser pass and that are not effected by the laser. This results in surface voids filled with raw material powder.
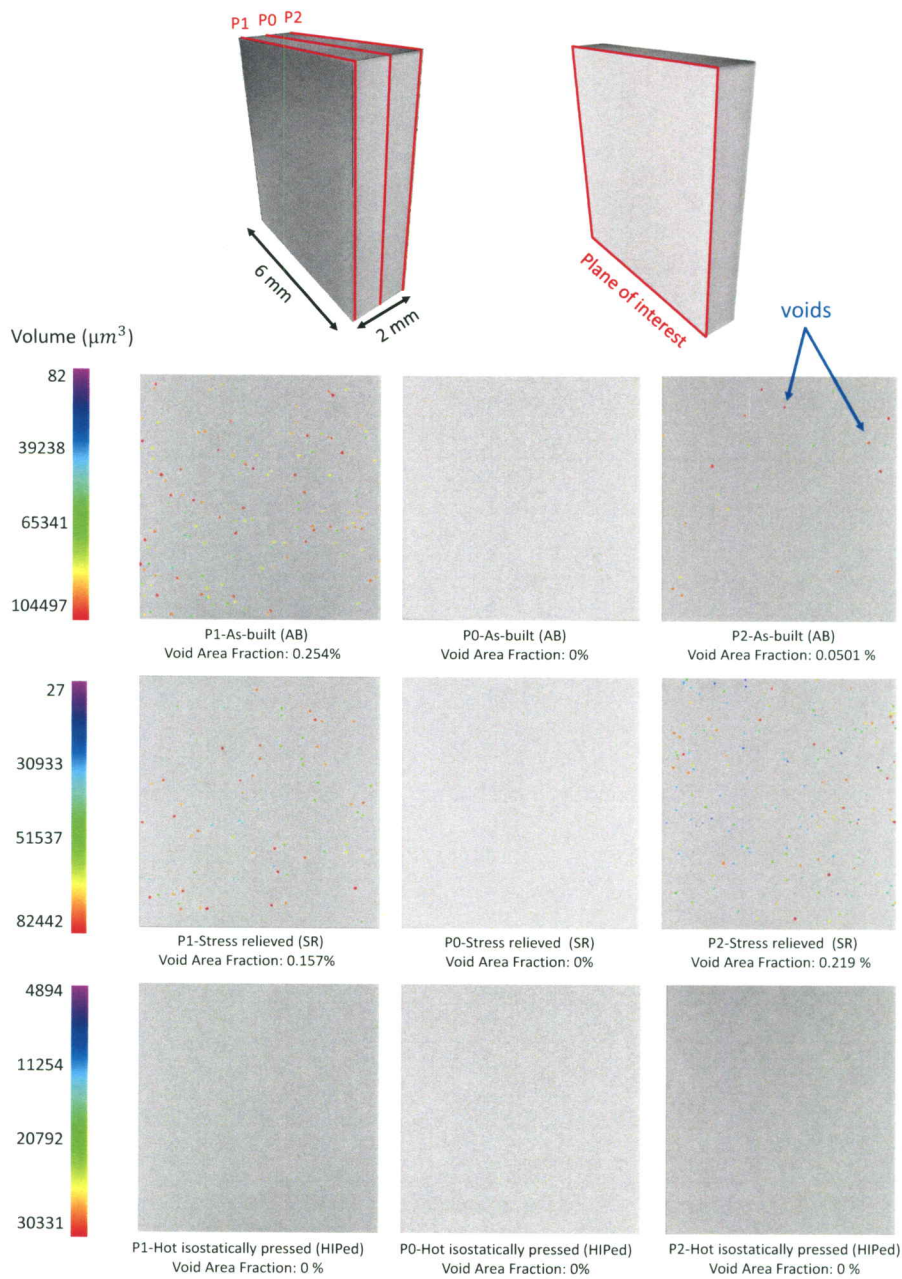
Figure 5.1: Comparison of the area fraction of porosity that forms along the transverse direction in the quasi static tension samples at AB, SR, and HIPed conditions. Presented scans represent the area fraction of the porosity (voids) for three arbitrary planes starting in the center of the sample and going 1 mm to either side.
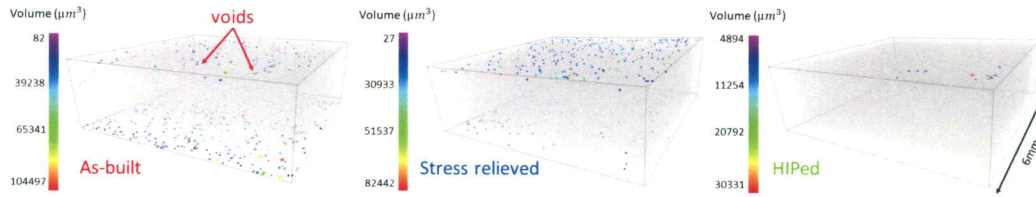
Figure 5.2: 3D Visualization of the CT Analysis. The volume shown represents the gauge section of the tension samples. Voids are shown in red and pointed out in blue. Voids were rarely viewed in the CT analysis in the HIPed sample.
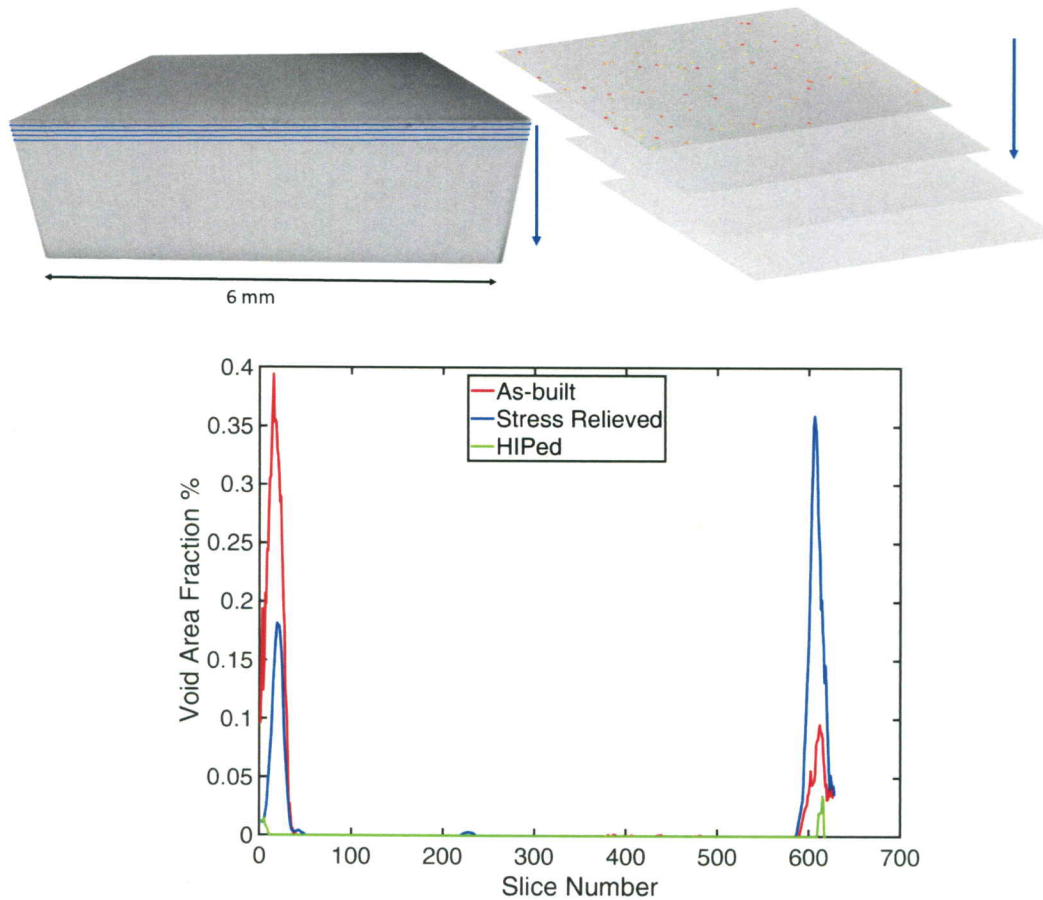
Figure 5.3: Void area fraction (void area of each slice divided by the total area of the slice) in the quasi static tension samples at AB, SR, and HIPed conditions for each slice in the build direction. The top image illustrates the gauge section of the quasi static tension samples and a visual representation of each slice and how they were taken.

5.2 Quasi-Static Testing

Bulk QS tests was preformed at room temperature for AB, SR, and HIPed heat treatments for both tension and compression. For the sake of consistency at least two tests were per-

36

formed at each condition. The compression and tension samples were loaded in the build direction outlined in Figure 5.4. Both the tension and compression samples deformed approximitely 6 ± 0.5 mm. At this deformation, the tension samples fractured. One Point Grey Grasshopper camera was positioned roughly 30 mm perpendicular to the speckled surface of the sample. This distance was determined by the focal point and so the entire sample is in the field of view. The Cole-Parmer illuminator was used to shine a light on the speckled faces of the sample.
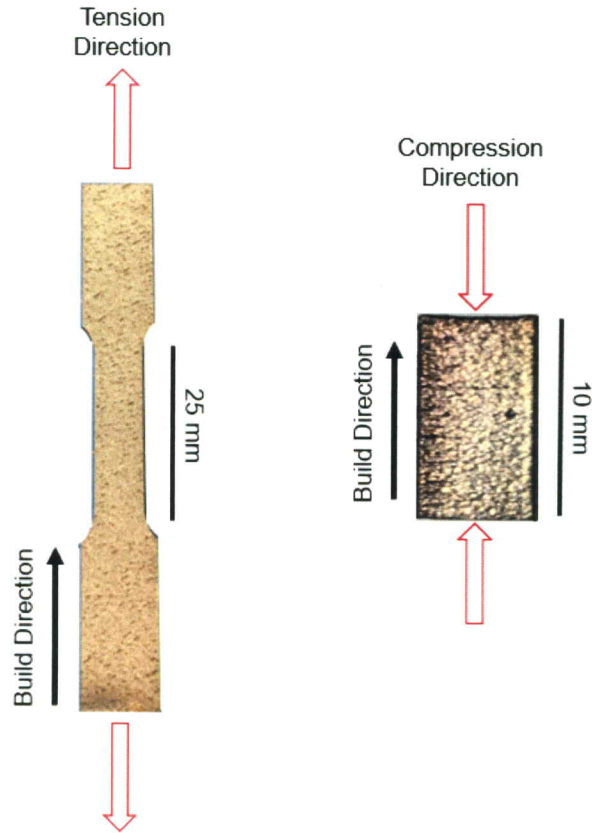
Figure 5.4: Experimental setup for the QS tension loading parallel to the build direction while the local strain was measured normal to the build direction.

It was assumed that the samples were isotropic so taking the strain at the surface of the sample represents the sample as a whole. The load was directly measured from the MTS machine. The stress is simply calculated by

$$\sigma = P/A \tag{5.1}$$

where P is the load and A is the cross sectional area of the sample.

Every time an image is taken, Vic Snap sends the information from the image into an excel file. This information contains the load, displacement, image count, and trigger. The load values for each image in the excel file is then uploaded into a MATLAB code where the stress is calculated. The images are uploaded into VIC2D [79] to run a DIC analysis to obtain the strain in the loading direction. DIC tracks the displacement of a speckle point in a reference image (the first image taken in the sequence when no load is applied) and

compares that point with the same point from a subsequent image. The engineering stress and strain values are plotted to give the compressive response of the material.

Figure 5.5a. demonstrates the QS compression behavior of AM IN718 after post processing heat treatment by showing the engineering stress-strain relationship. It is seen from Figure 5.5a that each compression sample for every heat treatment illustrates a novel behavior. Yielding for all three heat treatments occur around 0.01 engineering strain, followed by a gradual increase in stress until failure. The engineering strain increases about 17% as a result of the processing heat treatment induced by SR and HIPed. Each heat treatment has a critical strain point at which the strain comes to a halt while the stress continues to increase due to densification. For AB, this value is around 0.25 and 0.3 for both SR and HIPed. At this point, the sample reached maximum deformation but the load continued to be applied on the sample. The strain hardening rate remained the same for each heat treatment meaning the the strain hardening rate is insensitive to heat treatment at a low strain rate. Average flow stress was calculated by fitting a linear line between the yield point and the initiation of densification. From this calculation, it is seen that the flow stress increases around 20% as a result of the SR heat treatment and around 6% from the HIPed heat treatment.

Figure 5.5b. demonstrates the QS tension behavior of AM IN718 after post processing heat treatment by showing the engineering stress-strain relationship. Again, the QS tension behavior reacts about as expected. Yielding for all three heat treatments started around 0.01 engineering strain, followed by a steady increase in stress and strain until the ultimate tensile strength is achieved, then an abrupt decline until the sample fails. When the SR heat treatment is applied, the behavior mimics the AB behavior with the exception of an increase in flow stress of around 60 %. As for the HIPed heat treatment, there is also an increase in the flow stress, but the strain is decreased by 23%. Like in compression, it is shown that the strain hardening rate is insensitive to heat treatment at a low strain rate. The increase in mechanical properties from AB to SR reveals that porosity is more sensitive in tension than in compression.

Figure 5.6 and Figure 5.7 displays the QS compression and tension test with the corresponding instantaneous engineering stress-strain plot. The video on the left shows the speckled sample with the DIC strain map laid on top measuring the instantaneous strain in the loading direction. The red cross hair on the engineering stress-strain plot follows the curve while the samples are being deformed. The red dashed line falls on the engineering strain value at that instance, which is displayed at the bottom. At any instance during the deformation, the corresponding stress and strain can be visualized for analysis purposes.

(a)   (b)
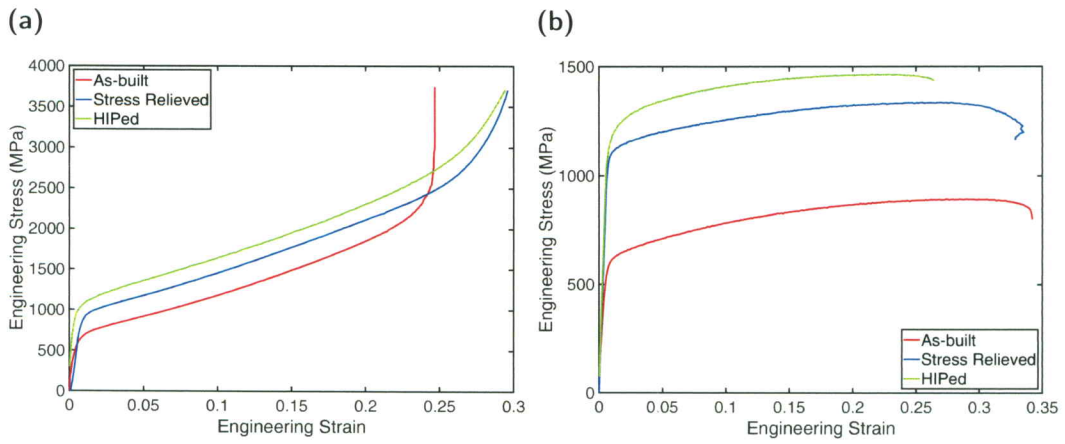
Figure 5.5: Engineering stress vs engineering strain plots are shown to describe the QS a) compression and b) tension behavior of AM IN718. The red line represents the AB behavior, blue represents the SR behavior, and green the HIPed behavior. Part a. shows the compression response and b. the tensile response.
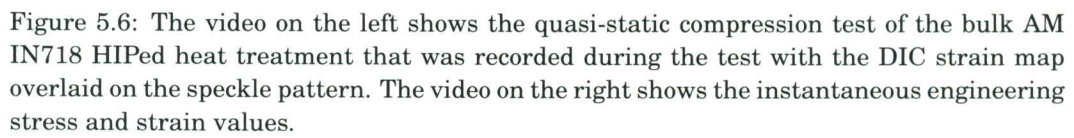
Figure 5.6: The video on the left shows the quasi-static compression test of the bulk AM IN718 HIPed heat treatment that was recorded during the test with the DIC strain map overlaid on the speckle pattern. The video on the right shows the instantaneous engineering stress and strain values.

Figure 5.7: The video on the left shows the quasi-static tension test of the bulk AM IN718 HIPed heat treatment that was recorded during the test with the DIC strain map overlaid on the speckle pattern. The video on the right shows the instantaneous engineering stress and strain values.

5.3 Dynamic Testing

Bulk dynamic testing was conducted using the Kolsky bar for AB, SR, and HIPed heat treatments for tension and compression at room temperature. During the test, multiple waves reverberated through the sample, but only the initial wave is considered in the analysis. The tension samples did not break from this initial pulse.

Typical analysis for Kolsky bar data uses an assumption of force equilibrium inside the sample simplifying the calculation of stress, strain, and strain rate [80, 81, 82, 83]. The forces at both faces of the sample can be obtained from the pulses measured by the strain gauges on the incident and transmit bar. The standard Kolsky bar analysis is based on the mechanics of the longitudinal elastic wave propagation in cylindrical bars [84]. Forces (P) at the transmission and incident bar sample interfaces are given by the following [85]:

$$P_I = E_b(\epsilon_I + \epsilon_R)A_b \tag{5.2}$$

41

$$P_T = E_b(\epsilon_T)A_b \tag{5.3}$$

Where ϵ_I, ϵ_R, ϵ_T is the incident, reflected, and the transmitted pulse strain obtained from the strain gauge measurements. A_b is the cross sectional area of the bar and E_b being the Young's modulus of elasticity and ρ_b the density of the material of the bar.

By assuming the sample stays under uniaxial stress, stress equilibrium, the bars undergo 1-D elastic wave propagation, the nominal strain rate, $\dot{\epsilon}_s$, nominal strain, ϵ_s, and nominal stress, σ_s, in the sample can be calculated using [85]

$$\dot{\epsilon}_s = \frac{-2c_b}{l_o}\epsilon_R(t) \tag{5.4}$$

$$\epsilon_s = \int_0^t \dot{\epsilon}_s(t)dt \tag{5.5}$$

Where c_b is the bar wave speed: $c_b = \sqrt{E_b/\rho_b}$ and l_o is the length of the sample respectively

Stress is dependent only on the transmitted wave when equilibrium is assumed in the sample. Equation (5.6) shows how stress in the sample as a function of time is calculated in the dynamic experiments.

$$\sigma_s(t) = \frac{E_b A_b}{A_s}\epsilon_T(t) \tag{5.6}$$

where A_s is the initial cross-sectional area of the sample.

Average stress in the sample can be calculated using Eq. (5.2) and Eq. (5.3) face forces values, instead of assuming a constant stress and is shown in Eq. (5.7).

$$\sigma_s(t)_{avg} = \frac{P_I(t) + P_T(t)}{2}\frac{1}{A_s} \tag{5.7}$$

The tension setup is similar to the compression testing with the exception of threaded tension grips required to hold the sample. The underlining principles of this tension arrangement is equivalent to the compression arrangement, except a tensile wave must be generated. This was done by firing a tubular striker bar at a cap threaded on the incident bar on the opposite end of the sample. The traditional way of calculating the tensile strain in the sample in the Kolsky bar gives an imprecise answer. In order to accurately measure the strain in the sample, the length of the sample needs to be known so the displacement measurement between the incident and transmission bar can be converted into strain. For compression, this length is easily obtained (simply just the length of the sample) but for tension, it is not well known since the instantaneous gauge length is hard to find due to the fillets and the clamps on the tension sample. The non–uniform deformation developed at these fillets contribute to the overall deformation of the sample [86]. Because of this, trying to figure out what length to use for the strain calculation can be difficult. To get around this issue, the ultra high-speed imaging Shimadzu HPV2 Camera using the SURE-Bright Fixed Focus LED light was used to illuminate the sample while the camera measures the sample displacement during the experiment. An open source software developed by REL called SURE-Pulse was used to calculate the stress and strain values.

The test samples fail depending on two factors: amplitude and duration of the wave. The amplitude comes from the velocity of the striker bar which correlates to the amount of pressure in the gas chamber, and the duration comes from the length of the striker bar (the longer the bar, the longer the duration). For this experiment, the gas chamber was pressurized with air to 100 psi and used a 610 mm striker bar. This pressure and striker bar length was chosen because through several experiments, it was obvious that the samples were not

easily broken. Therefore, the maximum pressure and longest striker bar was used. A momentum trap was placed on the incident bar to ensure that the sample is loaded only once instead of a repeated load. This is important so the initial, single pulse is observed because after the first pulse, the sample deforms into the plastic regime so the measurements after the first pulse are not useful for this experiment.

Figure 6.4 demonstrates the dynamic behavior of bulk AM IN718 after post processing heat treatments by comparing the engineering stress-strain relationship. These engineering stress and strain values are plotted from SURE-pulse. The lines from the plot are not smooth like the QS plots in Section 5.2. This is because the stress and strain data are derived from the waveform through the sample resulting in a rugged line produced in the plot. The end of each line in both the compression and tension plots does not indicate sample failure but the end of the initial compression and tension pulse. The samples did not fracture, but did undergo plastic deformation.

Figure 6.4a. represents the dynamic compression behavior of bulk AM IN718 at the various post processing heat treatments. Much like the QS behavior, yielding occurs around 0.01 engineering strain for all three heat treatments, followed by a gradual increase in stress and strain until the failure point was achieved. When the samples were subjected to the SR heat treatment, there was an increase in flow stress of around 25% and an increase in engineering strain of 15%. Alternatively, whenever subjected to the HIP heat treatment, the flow stress increased by around 6% and the engineering strain decreased 15%.

Figure 6.4b. represents the dynamic tension behavior of bulk AM IN718 at the various post processing heat treatments. Yielding occurs around 0.01-0.02 engineering strain for all three heat treatments, followed by a steady increase in stress and strain until the sample reached the failure point. There is a substantial increase in flow stress when the sample is subjected to the SR heat treatment, but also a 33% decrease in engineering strain. Furthermore, when the HIPed heat treatment is applied, there is an increase in flow stress of 6% and an increase in engineering strain of 33%.

The substantial increase in stress from AB to SR reiterates the conclusion that tension properties are more sensitive to porosity. Similar to the QS behavior, it can be observed that the strain hardening rate remained the same between heat treatments meaning the strain hardening rate is insensitive to heat treatment for higher strain rate as well. The decrease in mechanical properties from QS to dynamic reveals that porosity is more detrimental on the mechanical properties when the strain rate is increased.

Similar to the QS testing, Figure 5.9 and Figure 5.10 displays the dynamic compression and tension test with the corresponding instantaneous engineering stress-strain plot. The video on the left shows the speckled sample with the DIC strain map laid on top measuring the instantaneous strain in the loading direction. The red cross hair on the engineering stress-strain plot follows the curve while the samples are being deformed. The red dashed line falls on the engineering strain value at that instance, which is displayed at the bottom. At any instance during the deformation, the corresponding stress and strain can be visualized for analysis purposes.

(a)

(b)
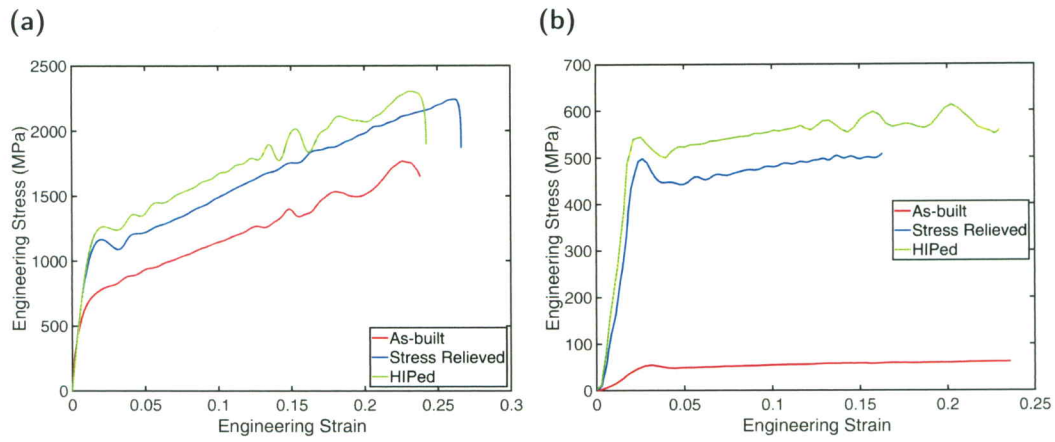
Figure 5.8: Engineering stress vs engineering strain plots are shown to describe the dynamic a) compression and b) tension behavior of AM IN718. The red line represents the AB behavior, blue represents the SR behavior, and green the HIPed behavior. Part a. shows the compression response and b. the tensile response.

Figure 5.9: The video on the left shows the dynamic compression test of the bulk AM IN718 HIPed heat treatment that was recorded during the test with the DIC strain map overlaid on the speckle pattern. The video on the right shows the instantaneous engineering stress and strain values.

Figure 5.10: The video on the left shows the dynamic tension test of the bulk AM IN718 SR heat treatment that was recorded during the test with the DIC strain map overlaid on the speckle pattern. The video on the right shows the instantaneous engineering stress and strain values.

Chapter 6

Lattice Structures

This chapter completes the story with the results from the X-ray CT and mechanical testing of the AM IN718 LS. A thorough discussion followed by the results are presented. The microstructure analysis is presented first in order to understand the effect of heat treatment on the microstructure within the struts and nodes. Then, the CT analysis is explained in detail which gives the ability to track the evolution of porosity throughout the struts and nodes. Following the CT analysis is the results from the QS and dynamic testing. The microstructure and CT analysis was presented before the QS and dynamic results in order to try to establish a relationship between the failure mechanisms and the corresponding microstructure and porosity distribution.

6.1   Lattice Structure Characteristics

LS are cellular structures that is a combination of solid material and gas-filled pores, which is a majority of the structure. As discussed in Section 3.2.2, four different topologies were investigated as shown in Figure 3.5: octet truss (OT), rhombic dodecahedron (RD), diamond (D), and dode-medium (DM). According to Maxwell's criterion [87], LS topologies can be divided into two main categories: (1) bending-dominated, and (2) stretching-dominated structures [88, 87]. From this, OT topology can be categorized as stretching-dominated, while the RD, D, and DM topologies are classified as bending-dominated. The effect of topology, unit cell size, and underlying strut microstructure on quasi-static and dynamic behavior was examined. For all topologies, the properties of the AB samples are compared with SR, HIP, and SA heat treatments.

6.2   Post Processing Microstructure Results

The different microstructures of the 4 mm unit cell size OT LS at AB, SR, HIPed, and SA heat treatment can be viewed in Figure 6.1. Here, the microstructure is defined as the grain size and morphology. OT is the only topology that has the struts and nodes in the same plane making this topology the best for microstructural analysis. Therefore, the 4 mm unit cell size sample can help relate the effect of the different heat treatments with the mechanical behavior observed in Figure 6.7.

It is reasonable to assume that microstructurally-driven events such as dislocation and porosity or geometrically-driven events such as strut buckling, macroscopic shear, and node cracking governs the deformation and mechanical strength in LS. In some topologies, for

example D topology with 2 mm unit cell size, altering the microstructure with the HIP heat treatment does not effect the mechanical strength potentially due to geometrically driven events dominating the deformation (see Figure 6.6d.). However, for the same topology with 4 mm unit cell size, since the HIP heat treatment increases the mechanical strength of the sample, this could mean that microstructurally-driven events dominate the governing deformation mechanisms (see Figure 6.7d.).
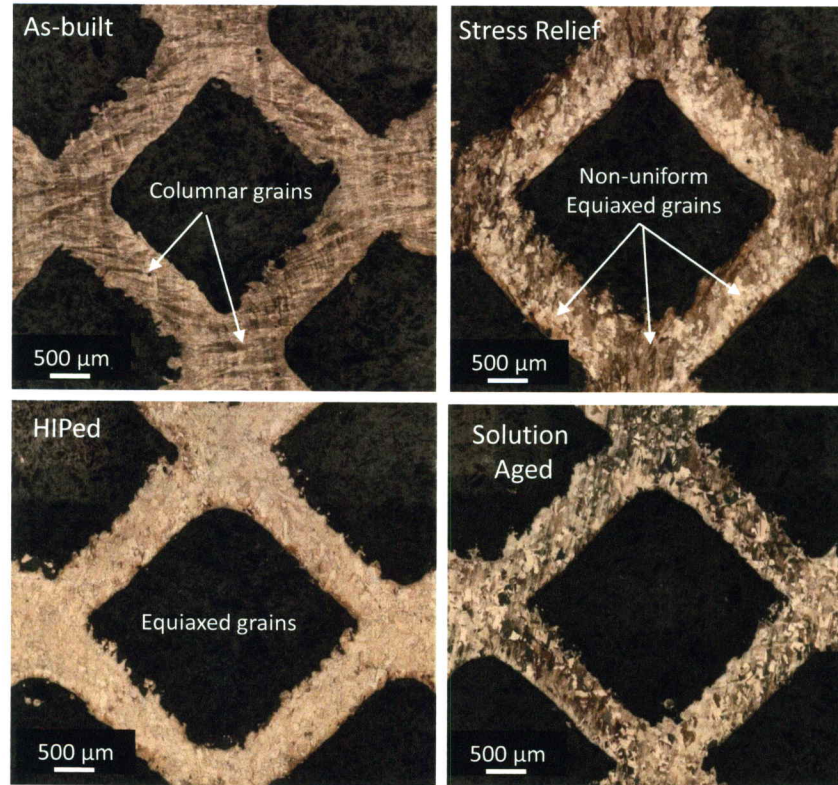
Figure 6.1: Comparison between the struts' microstructure of the AB, SR, HIPed, and SA samples of AM IN718 LS.

6.3 X-ray Computed Tomography

A volumetric X-ray CT investigation was conducted on 2mm unit cell size LS OT topology at AB, SR, and SA heat treatment conditions. The HIPed sample was omitted from this analysis due to limited resources and since it is expected that the SA heat treatment will have less porosity than the HIPed heat treatment. Table 6.1 outlines the total amount of porosity that was calculated for each heat treatment. It is shown from this table that the total number of voids decreased due to each heat treatment. Likewise, calculated void volume ratio decreased during the SR heat treatment. On the other hand, the void volume ratio remained constant in the SA sample. This is an interesting discovery because it is expected that a substantial decrease in voids would occur with when further HIP and SA heat treatments were applied. It is surprising that the porosity did not dramatically decrease with the HIP heat treatment process. This could be attributed from the empty space throughout the LS or the small diameter of the struts.

Table 6.1: Overall number of detected voids from the image analysis on X-ray scans for the 2 mm OT LS samples as a function of heat treatment.

Heat treatment	Total analyzed volume (μm^3)	Total number of voids	Total void volume ratio %
As Built	939,544,542,726	16568548	0.22
Stress Relieved	921,924,382,330	13284924	0.16
Solution Aged	937,579,988,048	12121288	0.16

Three arbitrary images normal (Figure 6.2) and transverse (Figure 6.3) to the build direction are shown in Figure 6.2 and Figure 6.3. These plains are pointed out in order to visualize the void distribution within the struts and nodes as the heat treatment varies. One of the observations from the study shows that the transverse direction produces a greater population of larger voids when comparing the difference in the porosity size and frequency along the transverse and build direction. Another observation was that for any given plane, the amount of porosity decreased when subjected to heat treatment. The primary reduction in the size and fraction of voids occurred during the SR heat treatment. From Table 6.1, it is shown that further HIP and SA heat treatments did not considerably reduce the void size and void volume fraction.

An analysis on the effect of the heat treatment on the area fraction of the voids are presented in Figure 6.4. The void area fraction for all the CT image slices cover the whole sample both normal (Figure 6.4a) and parallel (Figure 6.4b) to the build direction. Similar to the bulk response, it is observed from Figure 6.4b., the SR heat treatment increases the VAF in the transverse direction, but is then reduced with subsequent heat treatment. In general, the area fraction of the voids decrease as the heat treatment progresses in the build direction. Finally, it was also found that the nodes are more effective in eliminating porosity than in the struts for any given heat treatment advancement.
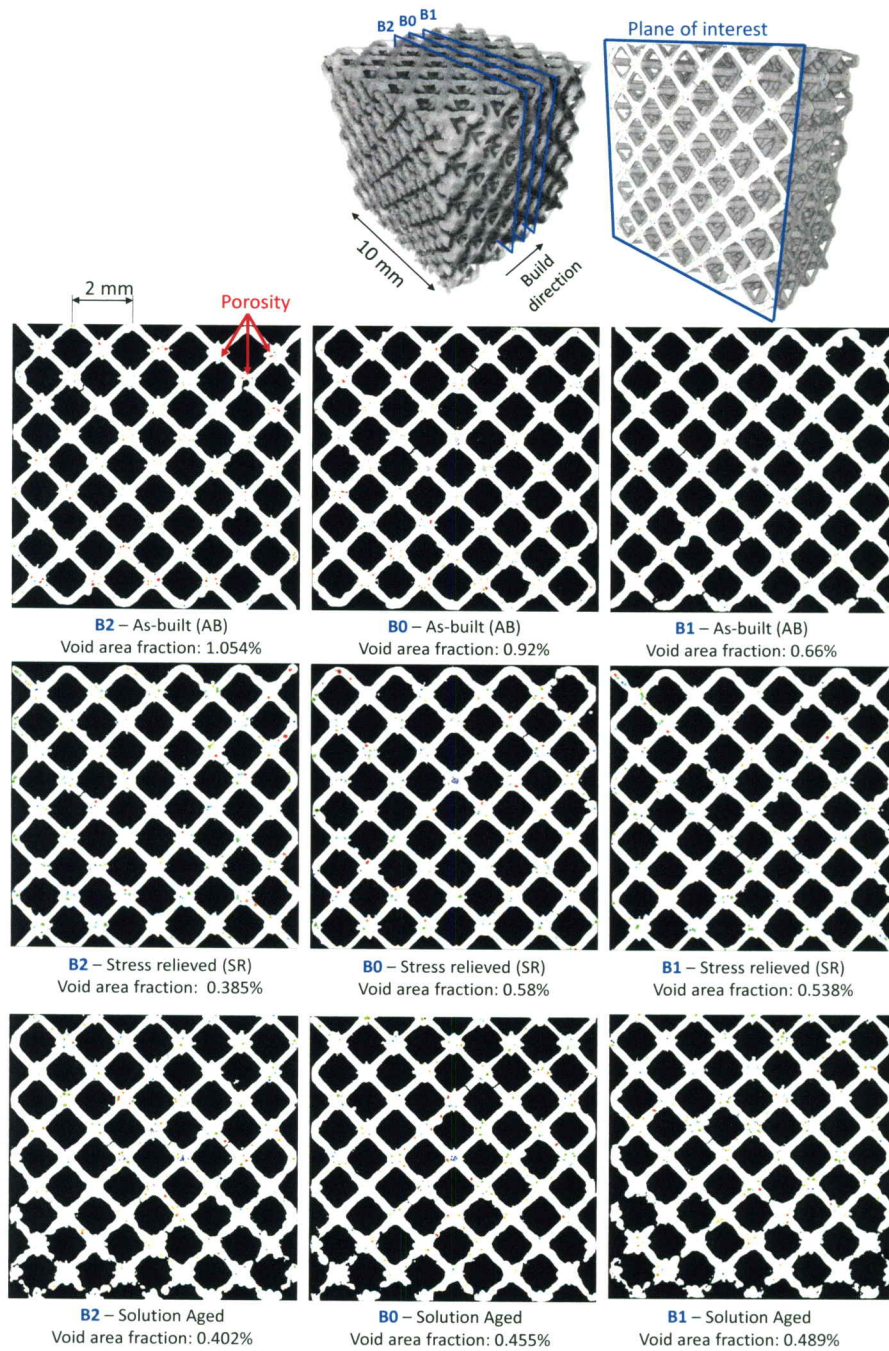
Figure 6.2: Comparison of the area fraction of porosity that forms along the build direction in the LS with octet truss topology at AB, ST, and SA conditions. Presented scans represent the area fraction of the porosity (voids) in the nodes and struts for three arbitrary planes starting in the center of the sample and going 1 mm to either side.
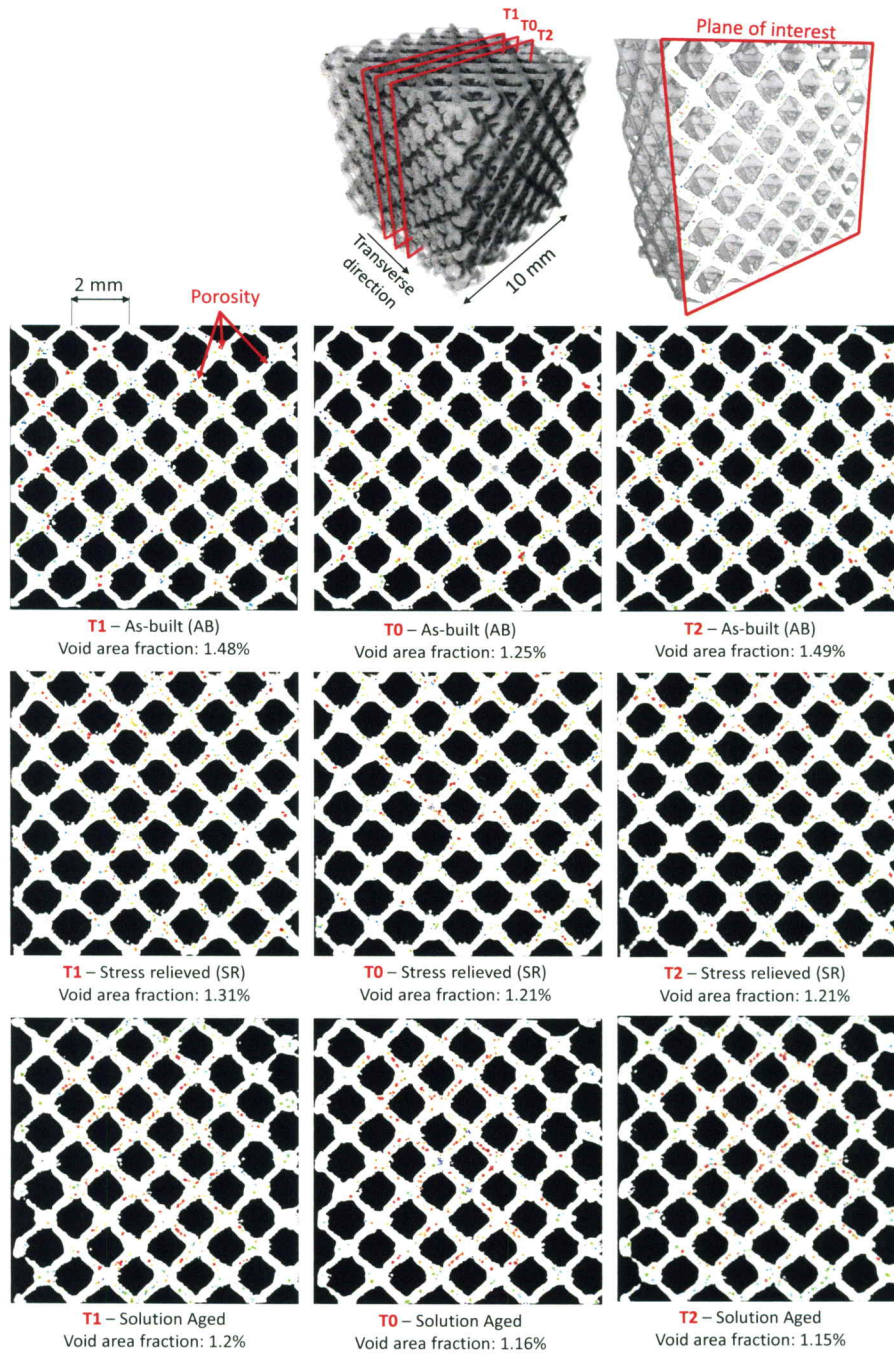
Figure 6.3: Comparison of the area fraction of porosity that forms transverse to the build direction in the LS with octet truss topology at AB, SR, and SA conditions. Presented scans represent the area fraction of the porosity (voids) in the nodes and struts for three arbitrary planes starting in the center of the sample and going 1 mm to either side.

(a)   (b)
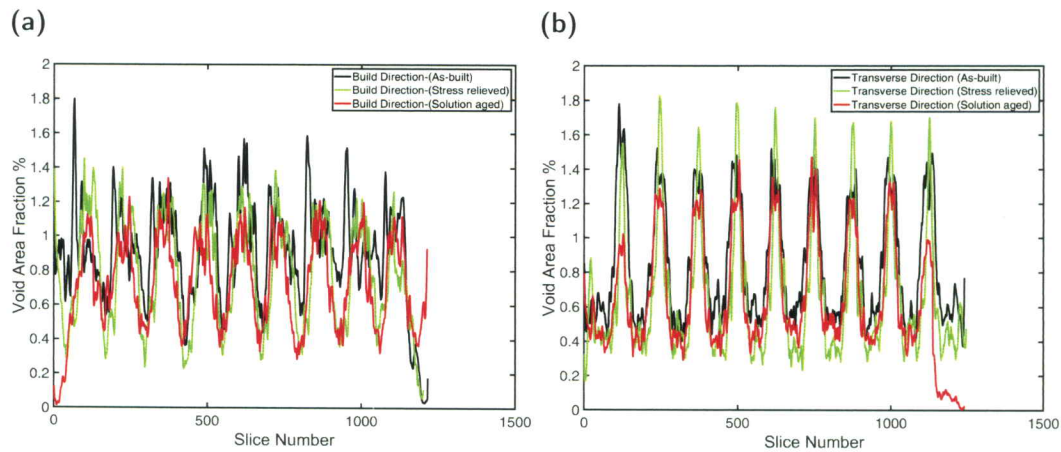
Figure 6.4: Void area fraction (void area of each slice divided by the total area of the slice) of octet truss topology at AB, SR, and SA condition for each slice in the build direction (a), and void area fraction of octet truss topology at AB, SR, and SA condition for each slice in the transverse direction (b).

6.4   Quasi-Static Testing

LS QS tests were performed on the same MTS machine at room temperature on all four toplogies with 2 mm and 4 mm unit cell sizes at AB, SR, HIPed, and SA condition. For the sake of consistency at least two tests were performed at each condition. Each sample was loaded in the transverse direction until the desired deformation was reached, 7 mm and 10 mm respectively for the 2 mm and 4 mm unit cell samples. Figure 6.5 shows a schematic of the QS loading setup and position of the cameras for OT sample with 4 mm unit cell size. Two Point Grey Grasshopper cameras were set up perpendicular to both of the speckled faces in the build and transverse directions (noted as camera 1 and camera 2).
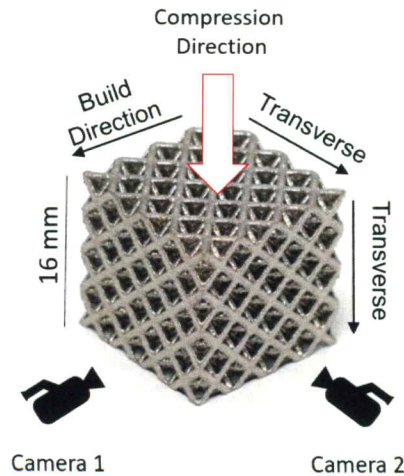
Figure 6.5: Experimental setup for measuring local strain on the face normal to the build direction (camera 2) and parallel to the build direction (camera 1) under quasi-static loading.

The same analysis was used to obtain the stress and strain as outlined in Section 5.2. Figure 6.6 demonstrates the QS LS 2 mm unit cell behavior of AM IN718 after post processing heat treatments by comparing the engineering stress-strain relationship for each topology. As seen from Figure 6.6, all heat treated topologies demonstrate a similar behavior. Yielding proceeds with a distinctive pattern with an increase in engineering stress until a total engineering strain of 0.1 to 0.2 is reached, followed by a slight decrease in stress. Subsequent rises in stress could be attributed to densification occurring within the LS [88].

From Figure 6.6a-c, it was observed that about a 45 % increase in the flow stress at 0.05 engineering strain occurred for the OT, RD, and DM topologies when subjected to SR heat treatment. In the same way, the flow stress stayed within 6 % of the SR value when subjected to the subsequent HIP and SA heat treatments. On the other hand, the D topology responded differently. In Figure 6.6d., it was observed that the HIPed heat treatment experienced a four time larger reduction in flow stress for the D topology than viewed on the other topologies. Similar trends were also observed under the dynamic loading (see Section 6.5). Therefore, the effect of the heat treatment on the flow stress of LS under QS loading cannot be generalized since deformation is also controlled by geometrical features.

Figure 6.6: The effect of post-processing heat treatment including SR, HIP, and SA on the quasi-static behavior of AM LS made of IN718, with 2 mm unit cell size, and fixed topology: (a) octet truss; (b) rhombic dodecahedron; (c) dode-medium; (d) diamond.

Figure 6.7 demonstrates the QS LS 4 mm unit cell behavior of AM IN718 after post processing heat treatments by comparing the engineering stress-strain relationship for each topology. The struts diameter increased from 0.344 mm to 0.689 mm from the 2 mm to the 4 mm unit cell size. The AB and SR conditions were investigated further due to the largest change in average flow stress values. Average flow stress was calculated by fitting a linear line between 0.05 and 0.5 engineering strain, which roughly represents the yield point and the initiation of densification. The average flow stress for the 4 mm unit cell size with OT, RD, DM, and D topologies increased by approximately 28%, 33%, 43%, and 31% respectively when subjected to SR heat treatment. Comparatively, the average flow stress increased for the 2 mm unit cell size for the OT, RD, DM, and D topologies was approximately 30%, 32%, 22%, and 21% respectively.

The 4 mm unit cell size LS showed a larger increase in average flow stress when compared to the 2 mm unit cell size after the SR heat treatment. As for the HIPed heat treatment, there was an insignificant change in the average flow stress in all instances except for the 2 mm unit cell size D topology. In this case, there was a 20 % decrease in flow stress due to the HIP process. Finally, there was a significantly different response to the SA heat treatment in the 4 mm unit cell size samples compared to the 2 mm samples. Flow stress increased by approximately 25 % as a result of the SA in the 4 mm samples whereas increases were less than 6 % in the 2 mm samples. This reveals that the larger unit cell size is more sensitive to heat treatment.

Post-yielding behavior in the 4 mm unit cell size samples had similar characteristics to 2 mm unit cell size samples. However, there were three key observations regarding the reduction in stress after surpassing the yield point:

1. The amount of stress reduction is greatest for the D topology.

2. The stress reduction is more sensitive to eat treatment.

3. The 4 mm unit cell size samples had a larger reduction in stress than the 2 mm unit cell sizes.

Figure 6.8 displays the QS 4 mm unit cell AB LS test with respect to both camera 1 and camera 2. The DIC strain map is projected onto the struts and nodes of the speckled sample. As the sample deforms, the DIC contour color changes due to the different strain values in the compression direction.
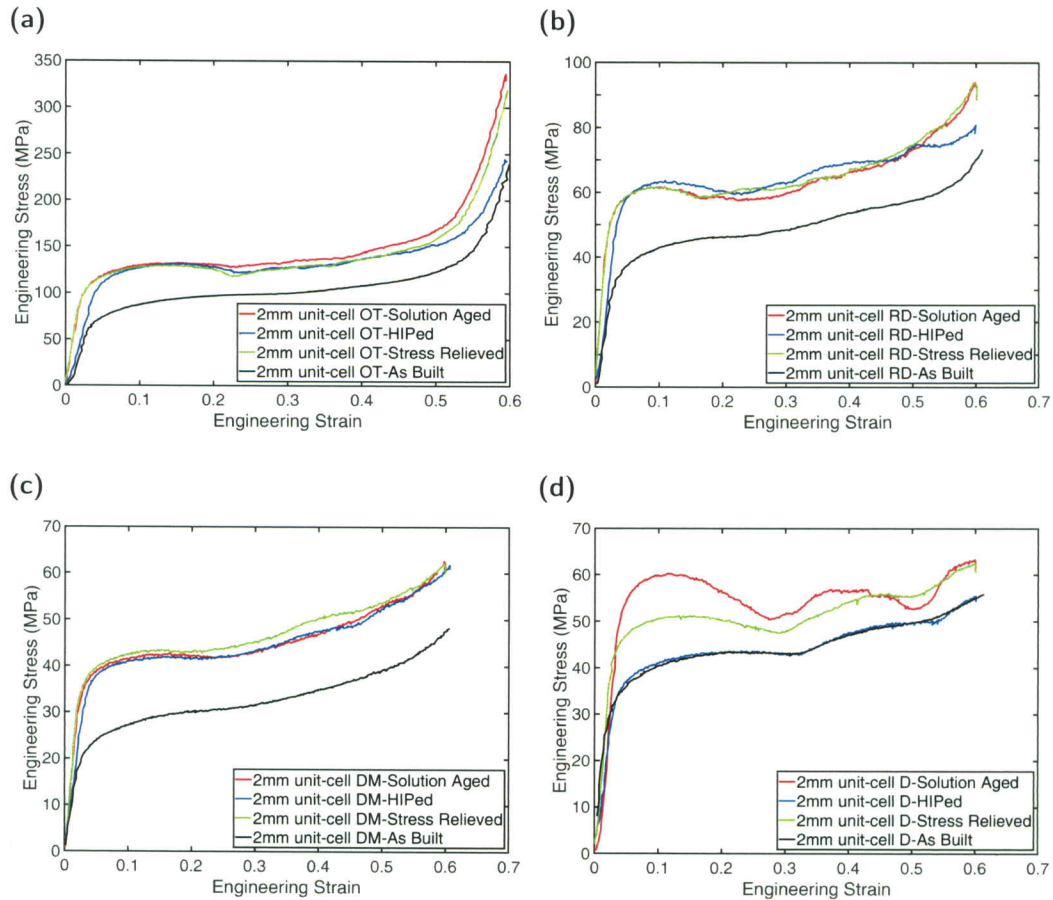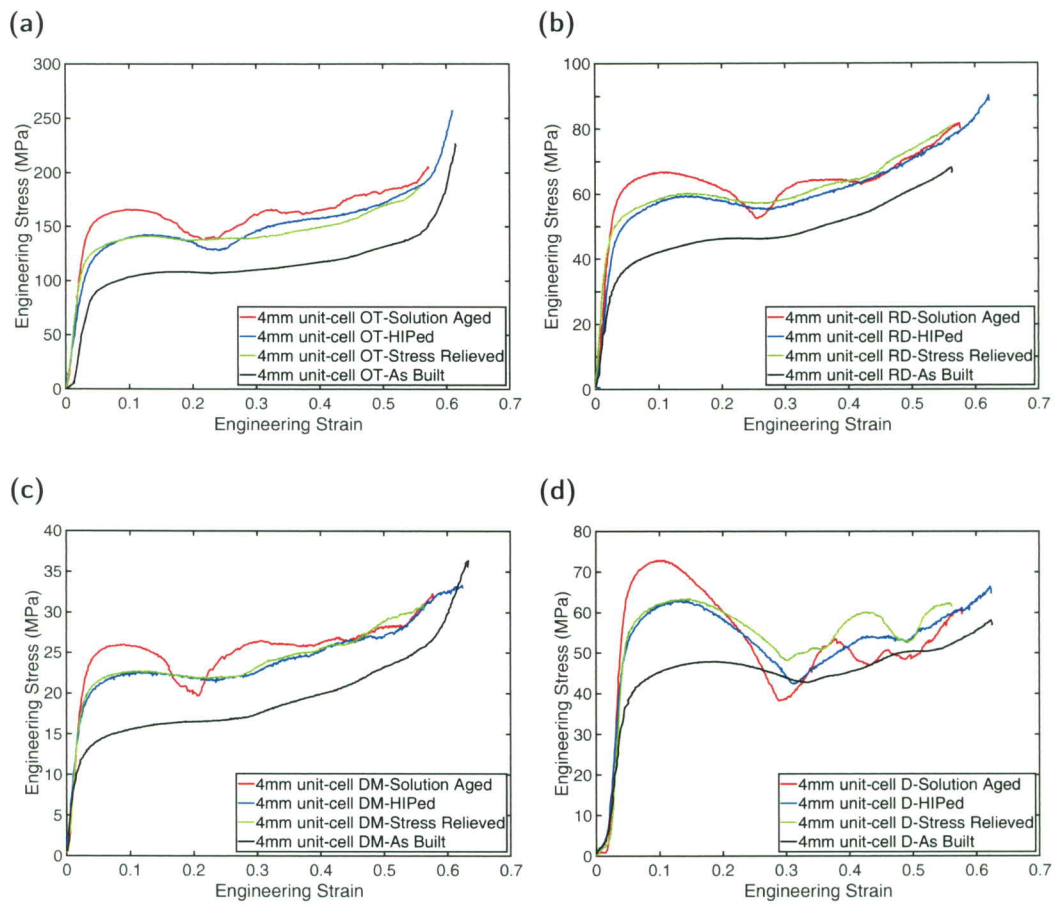
Figure 6.7: The effect of post-processing heat treatment including SR, HIP, and SA on the quasi-static behavior of AM LS made of IN718, with 4 mm unit cell size, and fixed topology: (a) octet truss; (b) rhombic dodecahedron; (c) dode-medium; (d) diamond.

Figure 6.8: Quasi-static compression of the OT LS 4 mm unit cell size as viewed from camera 1 and camera 2

6.5 Dynamic Testing

LS dynamic testing was conducted, at room temperature, using the Kolsky bar mentioned in section 4.5. Dynamic testing was carried out only on samples with 2 mm unit cell size. Reason being, the diameter of the Kolsky bar is not large enough to cover the entire 4 mm unit cell size samples. The corners of the samples were not in contact with the incident and transmit bars causing the wave to only go through a section of the sample.

The same analysis that was used in Section 5.3 was also used for the LS analysis. For the LS dynamic analysis, it was assumed that the cross-sectional area was as if the samples were fully dense. It was observed that the face forces, and hence the stress, achieved a reasonably equalized state during the dynamic tests thus confirming that the samples were in stress equilibrium. This analysis confirmed that it was viable to compare dynamic deformation trends between different topologies and heat treatment stages. Stress vs. strain results for dynamic deformation for the 2 mm unit cell size samples are shown in Fig. 6.9 in the form of nominal stress and global strain. Nominal stress refers to the stress in the sample using the entire cross-sectional area, assuming the sample was fully dense, and global

strain refers to engineering strain.

The 2 mm unit cell size samples in QS and dynamic showed similar behavior. From Figure 6.9a-c, it was observed that about a 40 % increase in the flow stress occurred for the OT, RD, and DM topologies when subjected to SR heat treatment. Similarly, the flow stress stayed within 6 % of the SR value when subjected to the subsequent HIP and SA heat treatments. On the other hand, the D topology responded differently as seen from Figure 6.9d. It was observed that an increase in the flow stress of 14% when subject to the SR heat treatment, a reduction of 20% in the flow stress as a result of the HIPed heat treatment, and an increase in 50 % in the flow stress for the SA heat treatment. Therefore, the effect of the heat treatment on the flow stress of LS under dynamic loading cannot be generally defined.

It was possible to compare between the quasi-static and dynamic results assuming that the assumptions used in the analysis described in Section 5.3 are correct. Discussion of these results are presented alongside the quasi-static results in Section 6.6.

(a)

(b)

(c)

(d)
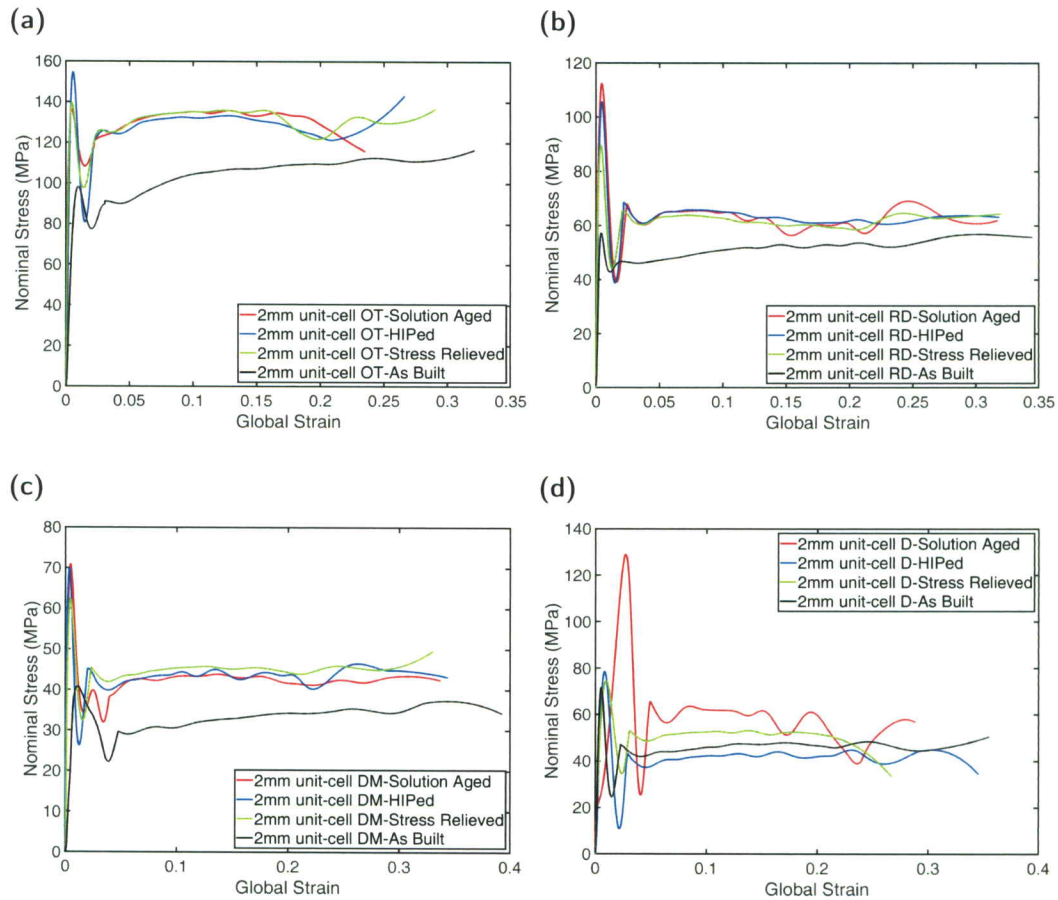
Figure 6.9: The effect of SR, HIP, and SA post processing heat treatments on the dynamic behavior of AM LS made of IN718, with 2 mm unit cell size, and fixed topology: (a) octet truss topology, (b) rhombic dodecahedron topology, (c) dode-medium topology, (d) diamond topology.

6.6 Comparing Quasi-Static and Dynamic Flow Stress Behavior

Flow stress behavior for both the 2 mm unit cell size LS QS and dynamic compression experiments are compared in Fig. 6.10. Trends regarding whether or not the initial magnitude of flow stress was increased or decreased due to the heat treatment type were independent of the strain rate. The maximum increase in flow stress was experienced between the AB and SR conditions, except in the D topology. On average for the OT, RD, and DM topologies, there was a 60 % flow stress increase due to the SR heat treatment during QS loading and a 40 % increase during dynamic loading, while the subsequent HIP and SA heat treatments changed the flow stress by less than 6 %. On the other hand, the D topology behaved differently in flow stress when subject to different heat treatments. The SR heat treatment increased the flow stress by 30 % and 20 % respectively for QS and dynamic strain rates. Interestingly, under QS loading, when the D topology was subjected to the HIPed heat treatment, a 20 % reduction in flow stress occurred. Under dynamic loading, the HIPed flow stress was lower than the AB value. Finally, the SA heat treatment resulted in an increase in flow stress of 16 % above the flow stress values in the SR condition for the D topology. These values are relatively large when compared to the nearly identical values of flow stress between the SR and SA samples for the other three topologies. This finding suggests that there is something inherently different about the deformation mechanisms in the D topology. This could mean that the D topology is geometrically driven whereas the OT, RD, and DM are microstructurally driven. Also observed was the flow stress for the dynamic experiments was greater for all topologies when compared to the QS experiments. The amount of strength increase due to dynamic loading was greatest for AB samples, around 20 %, but there was still an increase in strength for the other heat treatments, just not as significant. D topology samples experienced less of a strain rate effect compared to the other three topologies.

(a)

(b)

(c)

(d)
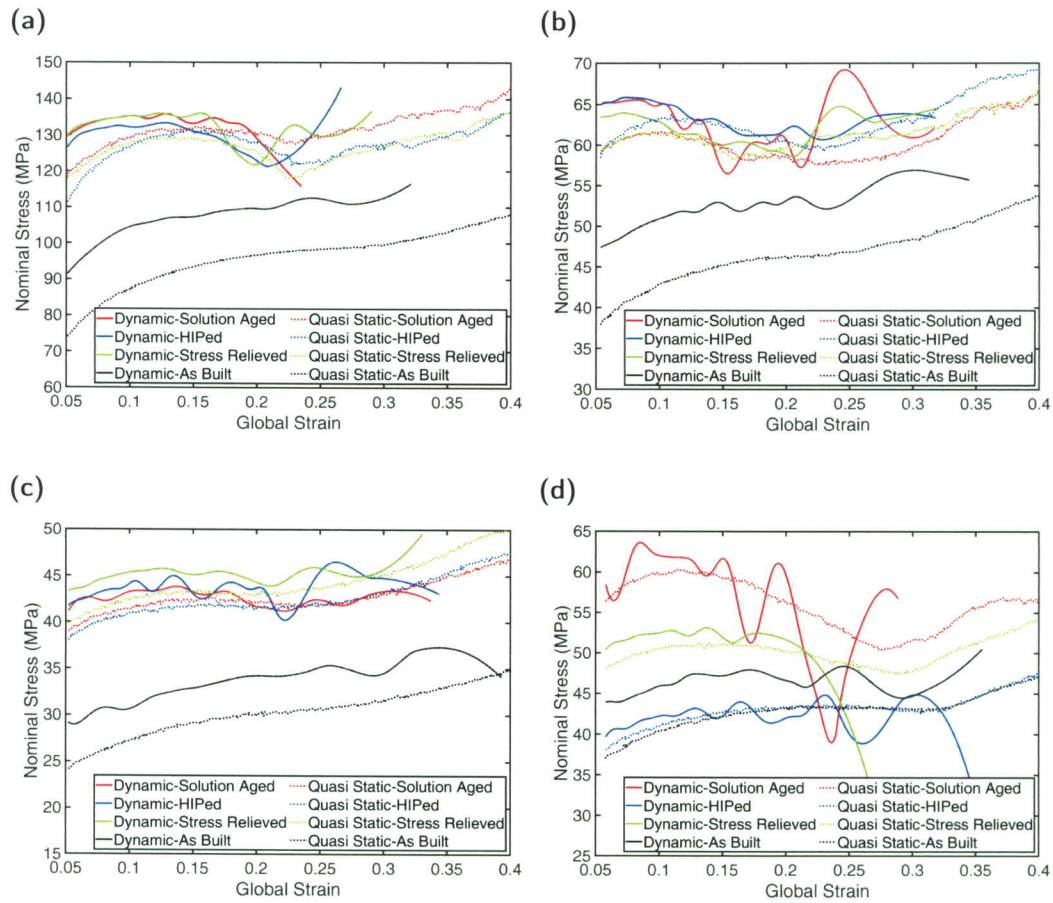
Figure 6.10: Quasi-static (dashed) and dynamic (solid) compression results for the 2 mm unit cell size LS at all heat treatment stages for: (a) octet truss topology, (b) rhombic dodecahedron topology, (c) dode-medium topology, (d) diamond topology. Plots begin after the dynamic experiments reach stress equilibrium. Each figure is plotted to different stress limits for the respective topology.

Chapter 7

Conclusion

This study quantified the evolution of microscopic porosity with respect to thermal post processing steps and their influence on the QS and dynamic behavior of AM IN718 bulk and LS. X-ray Micro CT was used to evaluate the post processing techniques to observe the amount of porosity in the AB, SR, HIP, and SA samples.

7.1 Bulk Sample Conclusions

The conclusions for the bulk samples are summarized as follows:

- Void size and frequency was dominant at the surface of the samples. The void number and percentage reduces with each heat treatment with AB having the highest percent (0.0148%) and HIP having the lowest (0.0003%). Interestingly, the SR heat treatment increased the number of voids at the bottom surface of the sample, which could be attributed from the heat treatment process causing the surface roughness to be increased, creating deep pockets on the surface, which are then corrected with the HIPed heat treatment because of the applied pressure, or it could be from not being able to control the sample preparation sanding to a fine tolerance.

- The strain hardening rate form both the quasi-static and dynamic tests remained the same between heat treatments. Therefore, the strain hardening rate is insensitive to heat treatment for both a low and high strain rate.

- From the mechanical results of the quasi-static and dynamic tension and compression test, the porosity effect was greatest in tension. The substantial increase in the mechanical properties from AB to SR in both quasi-static (60 % increase) and dynamic tension (900 % increase) reveals that the tensile properties are more sensitive to porosity than the compressive properties and also the SR heat treatment enhanced the quasi-static and dynamic strength to a greater extent than compared to the subsequent HIPed heat treatment.

- The decrease in mechanical properties from quasi-static to dynamic reveals that porosity is more detrimental on the mechanical properties when the strain rate is increased.

7.2 Lattice Structure Conclusions

The conclusions for the LS samples are summarized as follows:

- Void size and frequency was found to be greater transverse to the build direction. The results suggest the reduction of porosity between AB and SR heat treatments is greater compared to the reduction of the porosity when subjected to further heat treatments. Furthermore, porosity reduction was greater in the nodes than the struts when heat treatment was applied.

- For the octet truss, rhombic dodecahedron, and dode-medium topologies, the effect of microstructure in the yielding and plastic deformation behavior of LS became more dominant when the unit cell sizes were increased from 2 mm to 4 mm. With the 2 mm unit cell size, the SR heat treatment enhanced the QS strength by approximately 60 %. However, the subsequent HIP and SA heat treatments did not significantly increase the mechanical strength of the samples (only 6 %). Therefore, depending on the application of the part, the added cost associated with heat treatments further than SR might not be rational for the 2 mm unit cell size for only a slight strength increase. Alternatively, for the 4 mm unit cell size, the SA heat treatment had substantive effect on the mechanical strength by increasing flow stress by approximately 25 %. For the diamond topology, no matter the unit cell size, the SA heat treatment resulted in a flow stress increase.

- The tendency of the deformation of each topology were found to be independent of strain rate. For the 2 mm unit cell size octet truss, rhombic dodecahedron, and dode-medium topologies, the SR heat treatment resulted in the larger enhancement in flow stress with the quasi-static loading being 60 % and 40 % for the dynamic loading. The HIP and SA heat treatments produced nearly negligible flow stress changes of less than 6 %. The diamond topology experienced greater changes in the flow stresses due to the HIP and SR heat treatments with an approximate 10 % increase from the SR heat treatment and the hot isostatic pressed condition having a substantial flow stress decrease of 20 % from the SR heat treatment.

- The mechanical results of the 4 mm and 2 mm diamond topology LS indicate that deformation behavior is possibly controlled by different mechanisms than the other topologies.

Chapter 8

Future Work

Having successfully characterized the effect of porosity on the quasi-static and dynamic tension and compression properties on bulk IN718, alternative studies could include:

- Testing the samples under different loading conditions (e.g. fatigue, three-point bending) under the same heat treatments to see the impact (if any) porosity has on the mechanical properties.

- Testing the samples at elevated temperatures to see if the porosity effect is any different than at room temperature.

- Testing other highly used superalloys under the same testing conditions and heat treatments to characterize the porosity effect.

- Creating new samples through a different AM process to see what AM process produces the optimal mechanical properties.

As for the LS, this research clarified that different topologies respond differently to heat treatments effecting the mechanical properties of AM IN718, and that the behavior of the failure mechanisms of LS are difficult to generalize since, for instance, the diamond topology reacts differently than the other topologies. Further research could include:

- Testing the LS at the same heat treatments but in tension rather than compression. This can be preformed by creating a dogbone sample with the gauge section made of the LS.

- Dynamically testing the 4 mm unit cell size samples and compare the results with the dynamic 2 mm unit cell size samples and the quasi-static 4 mm unit cell size samples to see if there are any similarities or discrepancies in the data.

- Creating new LS samples with different unit cell sizes, for instance 3 mm and 5 mm, to observe the evolution of mechanical properties, if any, at a series of unit cell sizes ranging from 2 mm to 5 mm.

- Testing IN718 LS at several different AM processes only at the SR heat treatment to try and determine the best additive process for this material.

The few that are mentioned only include mechanical testing, not to mention studying the different types of failure mechanisms like the ones mentioned in Section 1.4.1 and 1.4.2, the electric properties, characterization methods, etc. There is an endless amount of work that can be done on AM IN718 bulk and LS.

Bibliography

[1] M.J. Bots. Energy Absorption of Additively Manufactured Lattices. *Master Thesis*, 01:01–77, 2017.

[2] M. Diehl D. Yan F. Roters D. Raabe C. Tasan, J. Hoefnagels. Strain localization and damage in dual phase steels investigated by coupled in-situ deformation experiments and crystal plasticity simulations. *International Journal of Plasticity*, 63:198–210, 2014.

[3] N. Biswas, J. Ding, V. Balla, D. Field, A. Bandyopadhyay. Deformation and fracture behavior of laser processed dense and porous Ti6Al4V alloy under static and dynamic loading. *Materials Science and Engineering: A*, 549:213–221, 2012.

[4] H. Kokawa S. H. Park S. Hirano Y. Zhang, Y. Sato. Microstructural characteristics and mechanical properties of ti–6al–4v friction stir welds. *Materials Science and Engineering*, 485:448–455, 2008.

[5] Jian Li Wei Hu Yongle Ren Yanjie Qiu Wei He Jianjun Chen Jianlin Li, Cong Chen. Investigation on compressive behavior of cu-35ni-15al alloy at high temperatures. *Materials Science-Poland*, 32:341–349, 2014.

[6] M. Aydinoz, F. Brenne, M. Schaper, C. Schaak, W. Tillmann, J. Nellesen, T. Niendorf. On the microstructural and mechanical properties of post-treated additively manufactured Inconel 718 superalloy under quasi-static and cyclic loading. *Materials Science and Engineering: A*, 669:246–258, 2016.

[7] AZO Materials. Calculation of phase diagrams using the calphad method. https://www.azom.com/article.aspx?ArticleID=359. (accessed: 02.07.2019).

[8] Farinia Group. Why choosing inconel 718 for aerospace additive manufacturing? https://www.farinia.com/additive-manufacturing/3d-materials/inconel-718-aerospace-additive-manufacturing. (accessed: 02.04.2019).

[9] A. Astaneh-Asl. Reconnaissance of collapsed macarthur maze elevated freeway and collection of perishable data. *Materials Science-Poland*, 01:01–39, 2011.

[10] X. Gong, J. Lydon, K. Cooper, and K. Chou. Beam speed effects on Ti–6Al–4V microstructures in electron beam additive manufacturing. *Journal of Materials Research*, 29:1951–1959, 2014.

[11] X. Wu, J. Liang, J. Mei, C. Mitchell, P.S. Goodwin, and W. Voice. Microstructures of laser-deposited Ti–6Al–4V. *Materials Design*, 25:137–144, 2003.

[12] E. Winick. Additive manufacturing in the aerospace industry. https://www.engineering.com/AdvancedManufacturing/ArticleID/14218/Additive-Manufacturing-in-the-Aerospace-Industry.aspx.

[13] J. Conway. How additive manufacturing is transforming medical manufacturing. https://www.mpo-mag.com/issues/2015-07-01/view_columns/how-additive-manufacturing-is-transforming-medical-manufacturing. (accessed: 01.26.2019).

[14] Sarah Goehrke. Additive manufacturing is driving the future of the automotive industry. https://www.forbes.com/sites/sarahgoehrke/2018/12/05/additive-manufacturing-is-driving-the-future-of-the-automotive-industry/#8bf000675cc5. (accessed: 01.26.2019).

[15] Standard terminology for additive manufacturing technologies. *ASTM-International*, F2792-12a, 2012.

[16] Longborough University Research Group. About additive manufacturing: Sheet lamination. https://www.lboro.ac.uk/research/amrg/about/the7categoriesofadditivemanufacturing/sheetlamination/. (accessed: 02.08.2019).

[17] J. P. Kruth G. N. Levy, R. Schindel. Rapid manufacturing and rapid tooling with layer manufacturing (lm) technologies, state of the art and future perspectives. *Manufacturing Technologies*, 52:589–609, 2003.

[18] ExOne Digital Part Materialization. What is binder jetting? https://www.exone.com/Resources/Technology-Overview/What-is-Binder-Jetting. (accessed: 02.08.2019).

[19] W. J. Sames, F. A. List, S. Pannala, R. R. Dehoff S. S. Babu. The metallurgy and processing science of metal additive manufacturing. *International Materials Reviews*, 01:1–46, 2016.

[20] Longborough University Research Group. About additive manufacturing: Directed energy deposition. https://www.lboro.ac.uk/research/amrg/about/the7categoriesofadditivemanufacturing/directenergydeposition/. (accessed: 02.08.2019).

[21] A. Bandyopadhyay S. Bose L. O'Donoghue C. Charitidis S. Tofail, E.. Koumoulos. Additive manufacturing: scientific and technological challenges, market uptake and opportunities. *Materials Today*, 21:22–37, 2018.

[22] Mattias Miedzinski. *Materials for Additive Manufacturing by Direct Energy Deposition*. Master's thesis in Materials Engineering, 2017.

[23] V. Bhavar, P. Kattire, V. Patil, S. Khot, K. Gujar, R. Singh. A Review on Powder Bed Fusion Technology of Metal Additive Manufacturing . *Kalyani Centre for Technology and Innovation (KCTI)*, 2012.

[24] J. Ruan, T. E. Sparks, Z. Fan, J. K. Stroble, A. Panackal, F. Liou. A Review of Layer Based Manufacturing Processes for Metals. *Department of Mechanical and Aerospace Engineering, University of Missouri – Rolla.*, 2011.

[25] L.E. Murr E. Martinez P. Shindo J. Hernandez S. Collins F. Medina K.N. Amato, S.M. Gaytan. Microstructures and mechanical behavior of inconel 718 fabricated by selective laser melting. *Acta Materialia*, 38:2229–2239, 2012.

[26] N. Hopkinson K. Mumtaz, P. Erasenthiran. High density selective laser melting of waspaloy. *Materials Processing Technology*, 195:77–87, 2008.

[27] S. Ford, M. Despeisse. Additive manufacturing and sustainability: an exploratory study of the advantages and challenges. *Journal of Cleaner Production*, 37:1573–1587, 2016.

[28] M. Gebler, A.J.M. Uiterkamp, C. Visser. A global sustainability perspective on 3D printing technologies. *Energy Policy*, 74:158–168, 2014.

[29] E. Atzeni, A. Salm. Economics of additive manufacturing for end-usable metal parts. *International Journal Advanced Manufacturing Technology*, 62:1147–1158, 2012.

[30] F. Nadin. When is 3d printing the best solution for production? https://www.sculpteo.com/blog/2016/05/25/when-is-3d-printing-the-best-solution-for-production/. (accessed: 01.26.2019).

[31] S. Brand. 5 major benefits of additive manufacturing you should consider. https://www.cmtc.com/blog/benefits-of-additive-manufacturing. (accessed: 01.26.2019).

[32] M. Despeisse, S. Ford. The Role of Additive Manufacturing in Improving Resource Efficiency and Sustainability. *Centre for Technology Management*, 03:1–8, 2015.

[33] P. Dalton, C. Vaquette, B. Farrugia, T. Dargaville, T. Brown, D. Hutmacher. Electrospinning and additive manufacturing: converging technologies. *Royal Society of Chemistry*, 01:171–185, 2013.

[34] G. Adam, D. Zimmer. Design for Additive Manufacturing—Element transitions and aggregated structures. *CIRP Journal of Manufacturing Science and Technology*, 07:20–28, 2014.

[35] Jacob Schwartz. How 3d printing can replace traditional manufacturing — and how it can't. https://revpart.com/3d-vs-traditional-manufacturing/. (accessed: 01.25.2019).

[36] D. Bourell, B. Beaman, M. Leu, D. Rosenc. A Brief History of Additive Manufacturing and the 2009 Roadmap for Additive Manufacturing: Looking Back and Looking Ahead. *Centre for Technology Management*, 01:5–11, 2009.

[37] Kruth Jean-Pierre Mercelis, Peter. Residual stresses in selective laser sintering and selective laser melting. *Journal of Rapid Prototyping*, 12:254–265, 2006.

[38] P. Withers, H. K. Bhadeshia. Residual stress: Part 1 – Measurement techniques. *Materials Science and Technology*, 17:355–365, 2001.

[39] W. Liu, R. Kovacevic, F. Kong. Residual stress analysis and weld bead shape study in laser welding of high strength steel. *ASME 2013 International Manufacturing Science and Engineering Conference*.

[40] H. Sasahara. The effect on fatigue life of residual stress and surface hardness resulting from different cutting conditions of 0.45% C steel. *International Journal of Machine Tools Manufacture*, 45:131–136, 2005.

[41] L. Ebert. Effects of residual stresses upon design, fabrication and field service. *Journal of Rapid Prototyping*, 25:406–449, 1974.

[42] T. Inoue G. Totten, M. Howes. *Handbook of Residual Stress and Deformation of Steel*. The Materials Information Society, 2002.

[43] C. Ruud. A review of selected non-destructive methods for residual stress measurement. *NDT International*, 15:15–23, 1982.

[44] M. Deveci. Measurement methods of residual stresses. https://www.stresstech.com/en-fi/know-how/articles/ stresstech-bulletin-12-measurement-methods-residual-stresses/. (accessed: 01.27.2019).

[45] P. Colegrove, H. Coules, J. Fairman, F. Martina, T. Kashoob, H. Mamash, L. Cozzolino. Microstructure and residual stress improvement in wire and arc additively manufactured parts through high-pressure rolling. *Journal of Materials Processing Technology*, 231:1782–1791, 2013.

[46] B. Szost, S. Terzi, F. Martina, D. Boisselier, A. Prytuliak, T. Pirling, M. Hofmann, D. Jarvis. A comparative study of additive manufacturing techniques: Residual stress and microstructural analysis of CLAD and WAAM printed Ti–6Al–4V components. *Materials Design*, 89:559–567, 2016.

[47] Zuback Mukherjee Elmer Milewski Beese Wilson-Heid De Zhang Roy, Wei. Additive manufacturing of metallic components–process, structure and properties. *Progress in Material Science*, 2017.

[48] Hwang Weng-Sing Huang Wei-Chin-Tsai Tsung-Wen Dezfoli, Ansari. Determination and controlling of grain structure of metals after laser incidence: Theoretical approach. *Sci. Reports*, 7:415–427, 2017.

[49] Copper Development Association Inc. Microstructures of copper and copper alloys. https://www.copper.org/resources/properties/microstructure/. (accessed: 01.27.2019).

[50] W. Ziaja J. Sieniawski R. Filip, K. Kubiak. The effect of microstructure on the mechanical properties of two-phase titanium alloys. *Journal of Materials Processing Technology*, 133:84–89, 2003.

[51] B. Pharm Y. Smith. What is optical microscopy? https://www.news-medical.net/ life-sciences/What-is-Optical-Microscopy.aspx. (accessed: 01.29.2019).

[52] R. Beanl P. Goodhew, J. Humphreys. Electron microscopy and analysis. 3:01–264, 2000.

[53] K. Leonard. Tem and electron diffraction. http://www.eng.uc.edu/~beaucag/ Classes/XRD/Labs/Keithhtml/Keith.html. (accessed: 01.29.2019).

[54] T. Körner Bauereiß, A. Scharowsky. Defect generation and propagation mechanism during additive manufacturing by selective beam melting. *Journal of Material Processing Technology*, 214:2522–2528, 2014.

[55] H. Castillo V. Gallegos G. Gibbs J. Hahn D. Kamath C. Rubenchik M. Alexander King, W. Barth. Observation of keyhole-mode laser melting in laser powder-bed fusion additive manufacturing. *Journal of Material Processing Technology*, 214:2915–2925, 2014.

[56] A. Rubenchik A. King E. Wayne Khairallah, S. Anderson. Laser powder-bed fusion additive manufacturing: Physics of complex melt flow and formation mechanisms of pores, spatter, and denudation zones. *Acta Materialia*, 108:36–45, 2016.

[57] F. Peter W. Babu S. Dehoff Sames, W. Medina. Effect of process control and powder quality on inconel 718 produced using electron beam melting. In *8th Int. Symp. Superalloy 718 Deriv*, pages 409–423, 2014.

[58] M. Courtois, M. Carin, P. Le Masson, S. Gaied, and M. Balabane. A new approach to compute multi-reflections of laser beam in a keyhole for heat transfer and fluid flow modelling in laser welding. *Applied Physics*, 46:505–516, 2013.

[59] M. Courtois, M. Carin, P. Le Masson, and S. Gaied. A two-dimensional axially-symmetric model of keyhole and melt pool dynamics during spot laser welding. *Rev. Métallurgie*, 110:165–173, 2013.

[60] Royal Society of Chemistry. Periodic table: Titanium. http://www.rsc.org/periodic-table/element/22/titanium. (accessed: 02.18.2019).

[61] H. Gong, K. Rafi, H. Gu, G.D.Janaki Ram, T. Starr, B. Stucker. Influence of defects on mechanical properties of Ti—6Al-–4 V components produced by selective laser melting and electron beam melting. *Materials and Design*, 86:545–554, 2015.

[62] S.Amin Yavari, S.M.Ahmadi, R.Wauthle, B.Pouran, J.Schrooten, H.Weinans, A.A.Zadpoor. Relationship between unit cell type and porosity and the fatigue behavior of selective laser melted meta-biomaterials. *Mechanical Behavior of Biomedical Materials*, 43:91–100, 2015.

[63] The Balance. The five sectors for steel applications. https://www.thebalance.com/steel-applications-2340171. (accessed: 02.18.2019).

[64] Holly D. Carlton, Abdel Haboub, Gilbert F. Gallegos, Dilworth Y. Parkinson, Alastair A. MacDowell. Damage evolution and failure mechanisms in additively manufactured stainless steel. *Materials Science and Engineering*, 651:406–414, 2016.

[65] Naci Kurgan. Effect of porosity and density on the mechanical and microstructural properties of sintered 316L stainless steel implant materials. *Material Design*, 55:235–241, 2014.

[66] Royal Society of Chemistry. Periodic table: Magnesium. http://www.rsc.org/periodic-table/element/12/magnesium. (accessed: 02.18.2019).

[67] H. Mayer, M. Papakyriacou, B. Zettl, S.E. Stanzl-Tschegg. Influence of porosity on the fatigue limit of die cast magnesium and aluminium alloys. *International Journal of Fatigue*, 25:245–256, 2003.

[68] S. Gangireddy, B. Gwalani, K. Liu, E. Faierson, R. Mishra. Microstructure and mechanical behavior of an additive manufactured (AM) WE43-Mg alloy. *Additive Manufacturing*, 26:53–64, 2019.

[69] T. Trosch, J. Strößner, R. Völkl, U. Glatzel. Microstructure and mechanical properties of selective laser melted Inconel 718 compared to forging and casting. *Materials Letters*, 164:428–431, 2016.

[70] M. Sangid, T. Book, D. Naragani, J. Rotell, P. Ravi, A. Finch, P. Kenesei, J. Park, H. Sharma, J. Almer. X. Xiao. Role of heat treatment and build orientation in the microstructure sensitive deformation characteristics of IN718 produced via SLM additive manufacturing. *Materials Letters*, 22:479–496, 2018.

[71] Ahmet T. I. Ozdemir A. Karaoglanli, K. Ogawa. Thermal shock and cycling behavior of thermal barrier coatings (tbcs) used in gas turbines. *Materials Science-Poland*, 01:238–257, 2013.

[72] Special Metals. Inconel alloy 718. `http://www.specialmetals.com/assets/smc/documents/inconel-alloy-718.pdf`. (accessed: 01.29.2019).

[73] T. Watkins, H. Bilheux, K. An, A. Payzant, R. Dehoff, C. Duty, W. Peter, C. Blue. Neutron Characterization for Additive Manufacturing. *Advance Material Processing*, 171:23–27, 2013.

[74] R. Reed L. Carter, M. Attallah. Laser powder bed fabrication of nickel-base superalloys: influence of parameters, characterisation, quantification and mitigation of cracking in superalloys. *Materials Science-Poland*, 32:577–586, 2012.

[75] Computational Thermodynamics. Calculation of phase diagrams using the calphad method. `http://www.calphad.com/nickel-chromium.html`. (accessed: 02.04.2019).

[76] G. Michael. X-ray computed tomography. *Medical Physics*, 10:442–451, 2001.

[77] X-Ray Energy and Attenuation. Ct physics: Beam hardening and dual-energy ct. `http://xrayphysics.com/dual_energy.html`. (accessed: 02.18.2019).

[78] N. Cuong, N. Minh, H. Cuong, P. Quoc, N. Anh, N. Hieu. Porosity Estimation from High Resolution CT SCAN Images of Rock Samples by Using Housfield Unit. *Scientific Research*, 8:1019–1026, 2018.

[79] Correlated Solutions. Principle of digital image correlation. `http://correlatedsolutions.com/digital-image-correlation/`. (accessed: 01.29.2019).

[80] Kaliat T. Ramesh. *Springer Handbook of Experimental Solid Mechanics*, chapter 33. High Rates and Impact Experiments, pages 929–959. Springer, 2008.

[81] Marc A. Meyers. *Dynamic Behavior of Materials*. Wiley-Interscience, 1994.

[82] Weinong W. Chen and Bo Song. *Split Hopkinson (Kolsky) Bar: Design, Testing and Applications*. Springer, 2011.

[83] George T. Gray, III. *ASM Handbook Volume 8: Mechanical Testing and Evaluation*, chapter Classic Split-Hopkinson Pressure Bar Testing, pages 462–476. ASM International, Materials Park, Ohio, 2000.

[84] H. Kolsky. An Investigation of the Mechanical Properties of Materials at Very High Strain Rates of Loading. *Proceeding of the Physical Society*, B62:676–700, 1949.

[85] K. T. Ramesh. Springer Handbook of Experimental Solid Mechanics: High Strain Rate and Impact Experiments. *https://www.springer.com/cda/content/document/cda–downloaddocument/9780387268835-c2.pdf?SGWID=0-0-45-545401-p107949126,*, accessed on 13 July 2018,:1–30, 2008.

[86] J. Harding, E.O. Wood, J.D. Campbell. Tensile testing of materials at impact rates of strain. *International Journal of Mechanical Sciences*, 2:88–96, 1960.

[87] M. Fleck Deshpande, V. Ashby. Foam topology: bending versus stretching dominated architectures. *Acta materialia*, 49:1035–1040, 2001.

[88] Lorna J Gibson and Michael F Ashby. *Cellular solids: structure and properties*. Cambridge university press, 1999.